Carlos Bartesaghi-Koc, Paul Osmond, Alan Peters

Innovative use of spatial regression models to predict the effects of green infrastructure on land surface temperatures

Energy and Buildings, 2022; 254:111564-1-111564-18

Final publication at: http://dx.doi.org/10.1016/j.enbuild.2021.111564

Innovative use of spatial regression models to predict the effects of green infrastructure on land surface temperatures

Abstract

Understanding the complex and dynamic interplay and cumulative effects of green infrastructure (GI) and urban form on land surface temperatures (LST) is important to design and implement heat mitigation strategies. Past research has mostly employed two-dimensional (2D) indicators, simple correlations and conventional regression models using coarse-level analytical approaches that obviate spatial autocorrelation effects. For the first time, this study applies a holistic approach to evaluate GI and urban settings as complex dynamic systems. The objectives of this paper are to: (1) develop novel 'spatially-based' predictive models that account for spatial dependencies; (2) implement a fine-scale analytical unit (<50m) for a more precise and accurate analysis; (3) incorporate the 'multi-temporal' diurnal and seasonal variations into predictions; and (4) propose the novel combination of 2D and 3D morphological, compositional and configurational parameters of GI and urban form derived from very high resolution (VHR) remotely-sensed data (<2m), using Sydney metropolitan region as case study. Results show a strong spatial association of LST at fine scale (<50m) and spatial autocorrelation among residuals in traditional models. Spatial error model (SEM) exhibits a superior performance over conventional multivariate regression, however, results presented significant heteroscedasticity caused by the large temperature variability in certain areas, although this problem was partially solved. Future studies should incorporate unmeasured factors related to material-specific properties (i.e. albedo, emissivity), and capture the thermal variation within urban areas by segmenting datasets into zones with relatively homogenous thermal and physical properties. Overall, ground imperviousness mostly defines the LST profile of a place, with a relative warming effect of 0.23°C and 0.61°C during day; and 0.18°C and 0.41°C at night per 10% of area increment in winter and summer, respectively. The same increment in the proportion of water and trees contributes to a maximum LST reduction of 0.42-0.85°C in summer, and 0.25-1.17°C in winter; however, this causes an increase of nocturnal LST between 0.12°C and 0.30°C throughout the year. In general, the cooling effects from GI do not outweigh the warming effects from man-made surfaces. Compared to abundance, the spatial configuration of trees is less influential on LST. Ground sky view factor (GSVF), altitude and distance to coast are of relative importance in defining LST profiles. These results used to numerically simulate different greening scenarios at neighbourhood scale for Sydney; illustrating the potential of spatial models to define heat mitigation scenarios to inform urban design and planning policies.

Keywords: Surface Urban Heat Island; Predictive modelling; Mitigation Strategies; Land Surface temperature; Spatial Error Model; Multivariate Regression; Ordinary Least Square Regressions.

Table of Nomenclature

AEDT	Australian Eastern Daylight Time
AIC	Akaike information criterion
BP	Breusch-Pagan
CBD	Central business district
CIRCLE_AM	Related circumscribing circle area weighted
D_Coast	Distance to the coast
DEM	Digital elevation model
DSM	Digital surface model
DW	Durbin-Watson
Fr_High_Veg	Fraction of high vegetation
Fr_Imp_Bld	Fraction of impervious building
Fr_Imp_Gr	Fraction of impervious ground
Fr_Low_NIR	Fraction of non-irrigated low vegetation
Fr_Low_IRR	Fraction of irrigated low vegetation
Fr_Med_Veg	Fraction of medium vegetation
Fr_Tot_Wat	Fraction of total water
GI	Green infrastructure
GLM	Generalised linear models
GSVF	Ground sky view factor
GWR	Geographically weighted regressions
H/W	Aspect ratio
JB	Jarque-Bera
KB	Koenker-Bassett
LAI	Leaf area index
LGA	Local government area
LiDAR	Light detection and ranging
LISA	Local Indicators of Spatial Association
LM	Lagrange Multiplier
Log-L	Log likelihood
LST	Land surface temperature
LULC	Land-use Land-cover
MCN	Multicollineatiy condition numbers
MLR	Multivariate linear regression
nDSM	Normalised digital surface model
NDVI	Normalised difference vegetation index
NEM	Normalised emissivity method
NIR	Near infrared
nLSI	Normalised landscape shape index
NN	Neural network
OLS	Ordinary least square
PCI	Park cool island
RNN	Recurrent neural network
RSVF	Roof sky view factor
SC	Schwarz criterion
S.E.	Standard error
SEM	Spatial error model
SLM	Spatial lag model
SRM	Spatial regression model
SUHI	Surface urban heat island
SVF	Sky view factor
TIR	Thermal infrared
UAV	Unmanned aerial vehicles
UCI	Urban cool island
UHI	Urban heat island
VHR	Very high resolution
VIF	Variance Inflation Factor

1 Introduction

Cities over the last century have experienced an unprecedented urbanisation process which has led to the radical territorial expansion of urban settlements [1]. This so-called urban sprawl is causing a significant loss of natural and agricultural landscapes, biodiversity and permeable soils which are replaced by impervious surfaces, buildings and roads [2, 3]. This land transformation can cause substantial variations in the surface energy balance, and consequently the rise of land surface temperatures (LST) [2]. This can be attributed to limited surface evaporation and moisture, increased solar absorption, increments of sensible heat fluxes, entrapment of long-wave radiation and abatement of air ventilation, which in turn are major stimuli for the intensification of surface urban heat islands (SUHIs) [4, 5].

Among several mitigation technologies, *green infrastructure* (GI) has been identified as a nature-based solution capable to mitigate urban overheating [6, 7]. Recent years have witnessed a significant growth in the number of remotely sensed studies focusing on the capacity of GI to ameliorate SUHIs, mostly due to the wide availability of satellite-derived imagery and the advent of unmanned aerial vehicles (UAVs) [8]. Studies have demonstrated that an increment in the abundance of well-irrigated vegetation cover leads to lower LST [9, 10]. However, what it is less known is the precise amount, composition and configuration of GI necessary to reduce LST and mitigate SUHI in more targeted ways [11, 12]. Thus, the accurate prediction of the thermal behaviour of urban greenery is becoming a high priority target in remotely-sensed climate research.

The motivation for this research is the apparent gap in knowledge regarding the complex interplay and cumulative effects of GI and urban form on the thermal environment. Earlier research has mostly implemented conventional regression models and simple correlations to analyse the relationships between GI and LST, without considering the non-stationary nature of these phenomena [13]. This implies a spatial dependence that compromises the reliability and predictive power of traditional models. Recent studies implementing spatially-based models have highlighted the importance of using finer analytical units (<100m), so a better theoretical basis for future urban regulations and landscape design can be provided [14].

For the first time, the present study applies a holistic approach to evaluate GI and urban areas as complex adaptive systems and proposes the innovative use of spatial regression models to address the dynamic nature of these phenomena and the issue of spatial autocorrelation. The objectives of this study are to: (1) specify and estimate novel 'spatially-based' predictive models that account for both the spatial neighbourhood effects and the simultaneous effects of various GI and urban morphology characteristics on LST; (2) implement a fine-scale analytical unit (<50m) for a more precise and accurate analysis; (3) incorporate the 'multi-temporal' diurnal and seasonal variations into predictions; and (4) propose the novel combination of multiple morphological, compositional and configurational urban parameters derived from 2D (i.e. thermal and spectral imagery) and 3D (i.e. LiDAR – light detection and ranging) very high resolution (VHR) (<2m) airborne-based data. The best produced models are then used to numerically simulate different SUHI mitigation scenarios at neighbourhood scale for the entire study area. This illustrates the potential of this integrated approach to better understand the fine-scale, complex and unique SUHI conditions across the Sydney metropolitan region, and to better inform greening interventions, urban design and planning policies in future.

2 Literature review

A large number of statistically-based forecasting approaches have been proposed to quantify and project the cooling effects of GI in the built environment. Most conventional quantitative analyses have implemented a two-dimensional (2D) approach. Numerous studies have explained and quantified the associations (correlations) between vegetation-derived characteristics and LST using Pearson's correlation, Spearman correlation, scattergrams, and curve fittings [15]. A set of studies have extensively compared biophysical parameters and indices – such as the normalised difference vegetation index (NDVI), or leaf area index (LAI) – and 'spectral-derived' surface or land characteristics (e.g. albedo, emissivity, land-use/land-covers – LULC, pervious surface fraction, percent of canopy cover, etc.) against the LST of a variety of analytical units such as pixel (or sub-pixel), regular grids, city blocks, or self-defined polygons. Furthermore, conventional regression approaches have focused on predicting LST based on one or multiple greenery-related variables by employing ordinary least square (OLS) [16, 17], multivariate linear regression (MLR) [18], multiple stepwise regression [19], generalised linear models (GLM) [12], elastic net regression [20], or principal component regression models [21].

On the other hand, studies applying a three-dimensional (3D) approach are scant, mostly because of limited data and technical challenges for their collection and processing [8]. These studies include urban morphology/geometry parameters such as sky view factor (SVF), aspect ratio (H/W), building and tree height, vegetation structure or stratification, orientation, altitude, and distance from coast [22, 23]. These aspects play an important role in the thermal performance of greenery as they affect air circulation, heat dissipation, and thermal energy absorption in open spaces and urban canyons [24, 25].

Other studies have employed spatial metrics such as FRAGSTATS [26] to examine the impact of morphology (e.g. shape, size, complexity), composition (variety, relative abundance) and configuration (arrangement, position, orientation, aggregation) of greenspaces and LULC types on the spatial variability of LST [27, 28]. Numerous studies have concentrated on the pattern and extent of urban/park cool islands (UCI/PCI) at large scales using space-borne thermal and spectral imagery [29–32]. It is consistently acknowledged that the morphology and composition of green patches are more influential on LST than their spatial configuration, and these relationships are scale-dependent [19, 33].

Several shortcomings have been identified in previous research. First, as noted before, remotely sensed research mostly relies on 2D information, putting aside many 3D morphological aspects of urban landscapes. Many studies have concentrated on a limited set of variables and investigations have been conducted within specific topics (e.g. studies using spatial metrics have excluded other variables); with notable exemptions [8, 12, 14, 18, 19, 34]. Therefore, there is an urgent need to implement a more holistic approach and protocols to evaluate the cumulative effects resulting from the interplay between natural and artificial features [35] by considering the built environment as a complex adaptive system [36, 37].

A very challenging situation occurs when temperatures are not only governed by 'internal' factors, but also by 'external' synoptic conditions to the site [38]. This is the case for Sydney, Australia, a coastal city that is affected by cool sea breezes that constantly compete against warm air advection from nearby desert landforms; causing a consistent gradient in LST across the entire city [39]. Approaches based on Artificial Intelligence (AI) are capable of dealing with this high complexity and variability, as well as with large number of input parameters and nonlinear relationships; aspects that are typically challenging for conventional prediction analysis. Examples of AI-based models employed for thermal prediction include Neural Network (NNs) [40–42], their recurrent variant (RNNs) [13] and hybrid models) [43]. Machine learning is a cutting-edge data-driven approach that requires specialised knowledge, otherwise results are prone to extensive criticism (i.e. hyper-sensitivity to weights, over-manipulation of parameters and overfitting) [13]. Although AI-based models are gaining ground in the field of urban heat island (UHI) forecasting, these models primarily concentrate on the accuracy of predictions (or outcomes) by relying on historical temperature trends, and tend to put aside the estimation of the specific contribution of each parameter to the overall thermal profile of the site investigated.

Second, multi-scale [8, 14, 27, 30, 44], multi-temporal [27], and fine-scale investigations [7, 12] are scarce. Due to the free accessibility to space-borne imagery, most remote sensing research has focused on medium and coarse resolutions (30-1000m) and daytime conditions. However, this is not suitable for describing the fine-scale characteristics and dynamic spatio-temporal thermal behaviour of urban greenery [45, 46]. This greatly limits the predictive capacity of models at the local-scale as relationships between LST and vegetation parameters highly vary in space and time [12]. In fact, prediction of the effect of greenery at the neighbourhood level (and nighttime) are urgently required as this is the scale that is more pertinent to city planners, urban designers and developers [47, 48].

Third, in relation to the above, conventional regression models are suited when the mutual relationships between LST and predictors are fairly constant or show a persistent pattern over space and time [13]; hence, they are limited in their ability to capture non-stationary phenomena as they exclude the spatial effects from nearby areas. This is also known as spatial dependence; observations from one particular place are related to the characteristics of adjacent places [49]. Moreover, LSTs are spatially autocorrelated or mutually dependent due to continuous surface heat fluxes [30]. Since spatial autocorrelation violates the assumption of 'independence' of conventional statistical methods, some recent studies have implemented geographically weighted regressions (GWR) [50, 51] and spatial regression models (SRM) [8, 14, 30, 34, 44, 52, 53] with promising results. Moreover, spatially-based statistical approaches tend to be less data-intensive and computationally-complex than NN-based algorithms, so they are worth further exploration in future.

3 Study area

The study area is located in Sydney, Australia's biggest city with 5.3 million inhabitants [54]. Sydney is located on the south-eastern coast of the country (33°45'S latitude) and is characterised by mixed urban form dominated by low-medium density areas interspersed with greenspaces, brownfield, industrial land, and transport corridors. Forested areas predominately concentrate in the northern region and along rivers and creeks. Compact, dense and high-rise structures are mainly located in the local government areas (LGAs) of Sydney (A), Parramatta (B), Liverpool (C), Canterbury-Bankstown (D), North Sydney (E), Ryde (F), and Willoughby (G) (Figure 1).

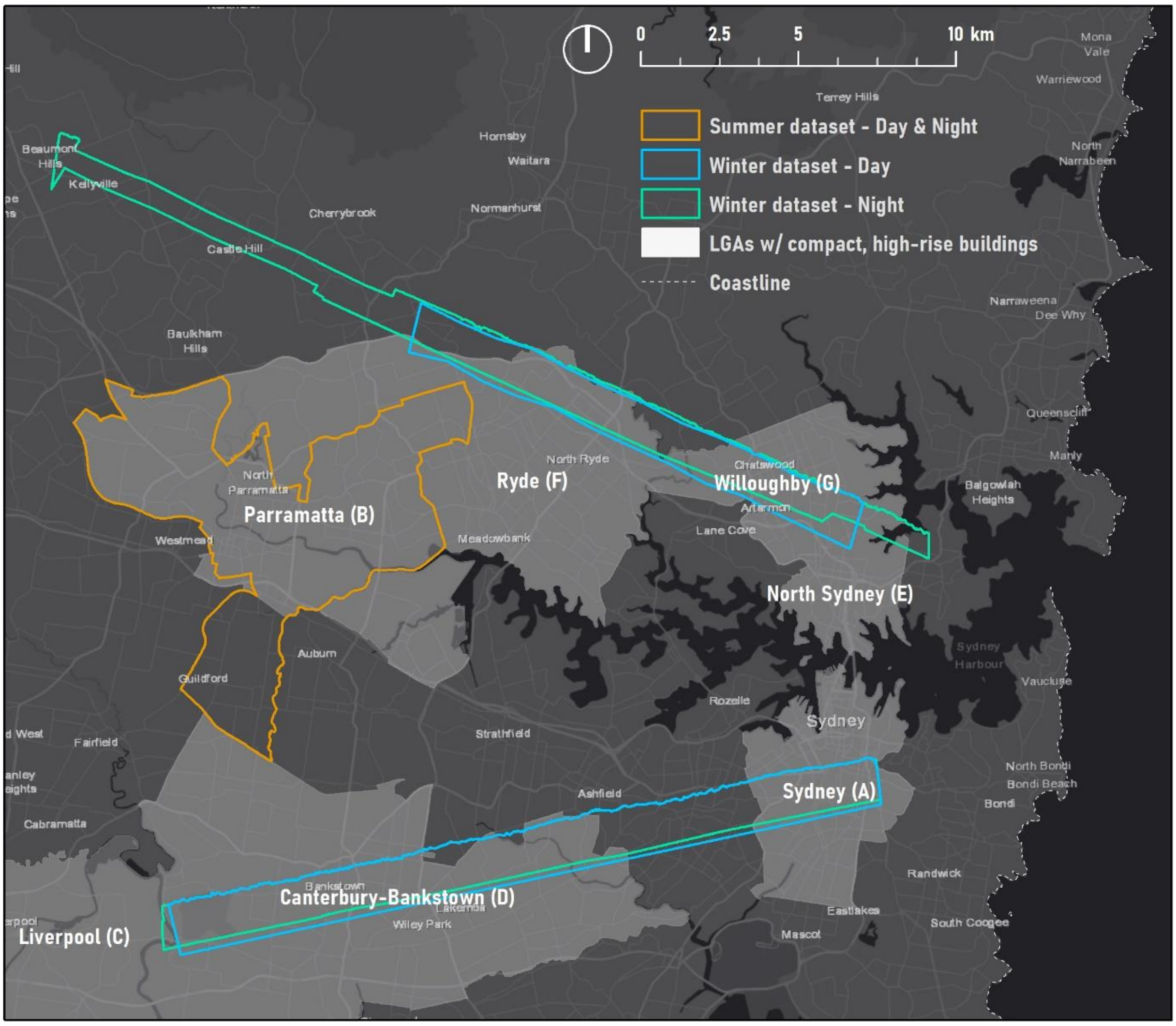

Figure 1. Sydney metropolitan region showing the differences in location and extent between the datasets derived from VHR airborne remote sensing data collected in summer and winter seasons.

Sydney exhibits a humid subtropical (*Cfa*) climate [55] with an annual monthly average temperature ranging from 16.4-26.0°C (data from Sydney's CBD between 1859-2018) [56]. Inland Western suburbs tend to exhibit daily average maximum and minimum temperatures considerably higher than those of Sydney's CBD (2°- 5°C), with an average of 45.5 days/year with temperatures above 30°C [56]. This pattern is associated with two specific synoptic systems; on one hand, easterly sea breezes from the ocean mostly dominate over the eastern suburbs and gradually reduce in intensity (wind speeds) towards the west. On the other hand, westerly winds –transporting warm/hot air from the interior– heat up the westernmost parts of the city [57]. Average rainfall patterns also follow a similar east-west gradient, with higher mean annual rainfall towards the north and east shores (>1200 mm/annum) and relatively drier conditions to the west and southwest (<900 mm/annum) [56]. Accordingly, the main reasons for selecting Sydney as case study are (1) the unique dualistic climatic pattern of the region, (2) the varied morphological and spatial characteristics, and (3) the prolonged urban overheating conditions experienced in recent years.

4 Methods

The methodological framework used in the present study follows the holistic views proposed by [37], and is based on the workflows applied by [58] and the data collection protocols implemented by [47]. The different steps performed in this study are presented in Figure 2 and a detailed explanation is provided in the following sections.

4.1 Data acquisition, processing, and computation of variables

The selection of statistical indicators was guided by the literature and this includes (1) multi-temporal LST (daytime and nighttime LST in summer and winter) as dependent variables; and (2) explanatory (independent) variables divided into three categories: functional, 2D/3D morphological, and configurational. A summary of data sources and their corresponding variables for the formulation of SRM is presented in Figure 2.

4.1.1 Land surface temperatures (LST)

Multi-temporal LST data were derived from airborne-based thermal infrared (TIR) imagery collected in two different seasons and times of the day, as it is increasingly important to produce numerical models suitable for various boundary and microclimatic conditions [59]. Ideally, datasets collected in different seasons should share the same spatial extent; however, in this study the acquisition of VHR airborne-based data (Figure 1) mainly responded to data availability, logistic issues (adequate weather and air traffic regulations), and budgetary limitations.

For summer, day TIR imagery (2.1m spatial resolution) was captured on 8 February 2013 between 1:36-2:20pm AEDT (Australian Eastern Daylight Time), while night TIR imagery (1.2m spatial resolution) was acquired between 11:24pm-12:58am AEDT. Both flights employed a FLIR A615 camera with an accuracy of ±2°C. For winter, both day and night TIR images (0.5m spatial resolution) were retrieved using a FLIR SC series camera on 6 August 2012 between 12:00-2:00pm AEDT, and on 4 August 2012 between 11:30pm-1:30am AEDT, respectively. The processing of TIR images was performed by contractors and included: (1) the ortho-rectification and geo-referencing using aerial photography; (2) the estimation of absolute LST using a normalised emissivity method (NEM) [60, 61] assuming a constant emissivity value of 0.96, (3) continuous mosaicking and resampling images to 1m pixel resolution; and (4) the creation of look-up tables with temperatures in Kelvin and Celsius (°C) degrees.

4.1.2 Normalised difference vegetation index (NDVI)

NDVI has been extensively employed to distinguish different surface covers (vegetated, impervious, water) and can be interpreted as a bio-physical (functional) indicator of vegetation performance (health) as it is strongly correlated to surface evapotranspiration [62–64]. Furthermore, NDVI can be associated with convective cooling and latent heat vaporisation when vegetation is under well ventilated conditions [8]. In this study, VHR NDVI raster images (1m resolution) for summer and winter were derived from the available multi- and hyper-spectral data respectively, by using the Visible (RED) and Near Infrared (NIR) reflectance bands in Eq. (1):

$$NDVI = \frac{NIR - RED}{NIR + RED} \qquad (1)$$

Multispectral imagery (4 spectral bands 450–780 nm) was captured in a flight campaign on 17 August 2013 using a SpecTerra's HiRAM sensor while hyperspectral imagery was captured on 6 August 2012 using a Norsk Elektro Optikk (NEO) VNIR1600 HySpex Camera (160 spectral bands 400–1000 nm). The pre-processing of spectral images was performed by the contractors and included: (1) radiometric and atmospheric corrections using Altair software, (2) ortho-rectification and georeferencing using ISAT software for triangulation and LPS software for ortho-photo correction; and (3) resampling all imagery to 1m pixel resolution.

4.1.3 2D/3D urban composition indicators – surface covers

To identify generic surface covers (vegetated, impervious, water) a NDVI threshold approach was applied: reclassifying pixel values of spectrally-derived NDVI images using thresholds predefined using the Jenks optimization method [65], and readjusted as per the literature [8, 66–68]. LiDAR point clouds were used as ancillary data to refine these spectrally-derived surface cover extractions. LiDAR data were retrieved from the ELVIS Geoscience portal (https://elevation.fsdf.org.au/) which were pre-classified according to the American Society of Photogrammetry and Remote Sensing (ASPRS) guidelines, into low vegetation or grasses (0–0.3m), medium vegetation or shrubs (0.3–2 m), high vegetation or trees (>2m), buildings, ground, and water. LiDAR data were acquired between 10 and 24 April 2013 using a Leica ALS50-II sensor scanner that generated LAS tiles of 2x2km with a nadir point density of 1.03/m^2 and an average point density of 1.57/m^2.

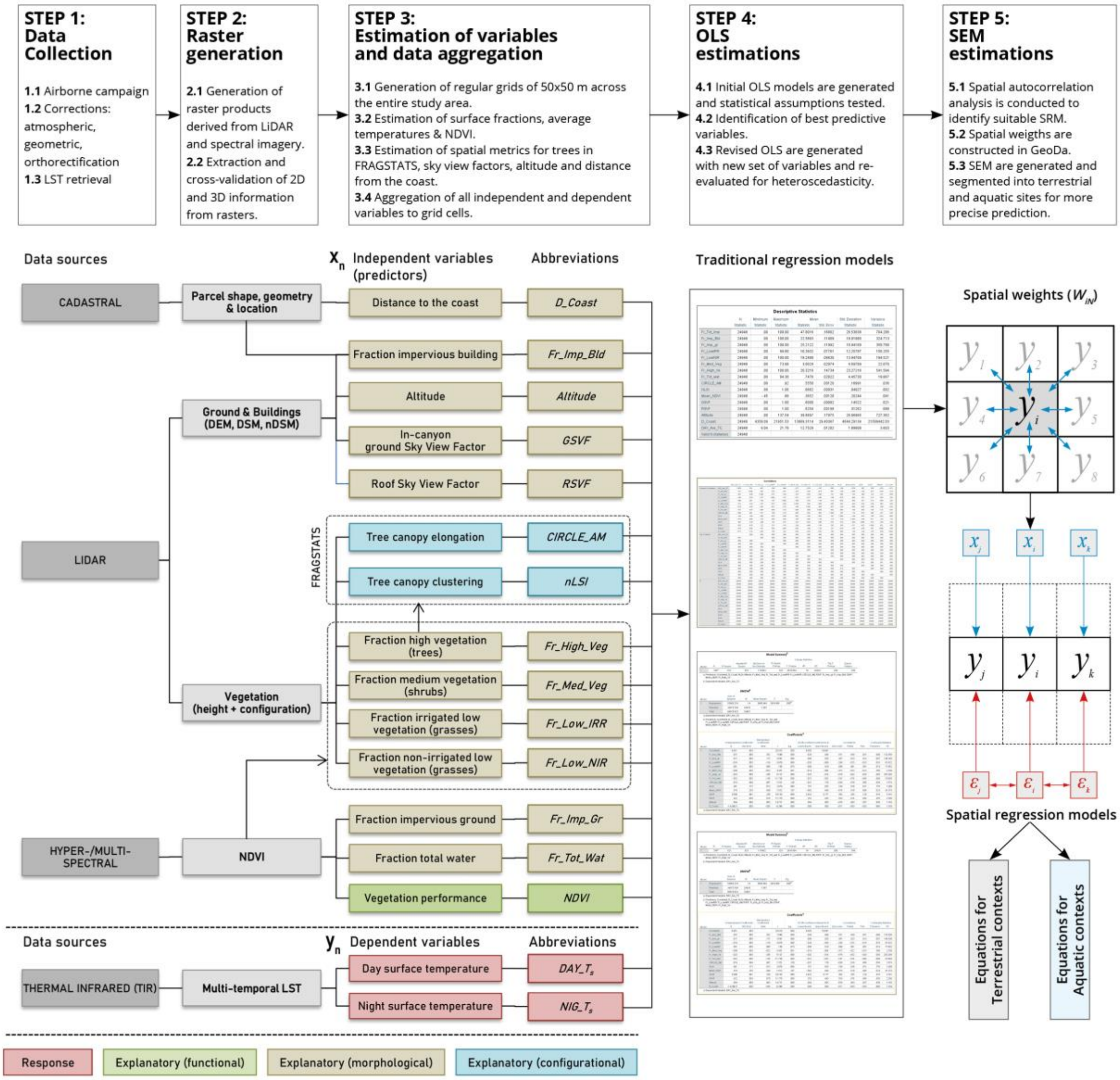

Figure 2. Holistic methodological framework showing the methods and steps applied in this study; the summary of data sources; and their corresponding dependent (response) and independent (explanatory) functional, morphological and configurational variables for the estimation of both traditional OLS models and SRM models.

Raster images corresponding to trees, shrubs, grasses and buildings were derived from LiDAR data using a point cloud tracing algorithm available in LP360 software [69]. Since various water regimes and seasonal variation (presence of deciduous trees) are expected across the study area, and to improve the spatial accuracy of estimations, additional corrections were applied by cross-validating LiDAR- and NDVI-derived raster images against each other, and doing this in multiple occasions and iteratively. Cadastral data including land tenures (parcel size) and geographical features (greenspaces, water bodies, coastline) were obtained from the data.gov.au portal [54] and employed to improve and validate previous calculations. LiDAR-based building footprints were split along property boundaries (parcels) and squared-up using an algorithm available in Feature Analyst® software. This process facilitated the precise discrimination between impervious ground and impervious building, water, irrigated and non-irrigated grasses, shrubs, and tree canopy. All surface covers were extracted in individual raster images of 1m pixel resolution.

4.1.4 3D urban morphology indicators – sky view factor (SVF), altitude, distance to coast

The SVF (ψ), is a unitless parameter[1] that can help quantifying the cooling of a space by measuring the proportion of the viewing hemisphere occupied by the sky in a specific point or over the entire area of a horizontal surface [70, 71]. SVF can be used as a 3D-based indicator of built form density and geometry that strongly influences the energy balance of urban surfaces due to potential solar exposure (and shading) influenced by natural (trees) and man-made structures (buildings) [72–74]. As suggested by [8], two types of SVF measures were computed: (1) ground SVF (*GSVF*) which describes the *in-canyon* obstructions of sky at pedestrian level which combine the actions from both buildings and trees, and (2) roof SVF (*RSVF*) which measures obstructions of sky on buildings' roof that may be affected by taller natural or artificial features (Figure 3).

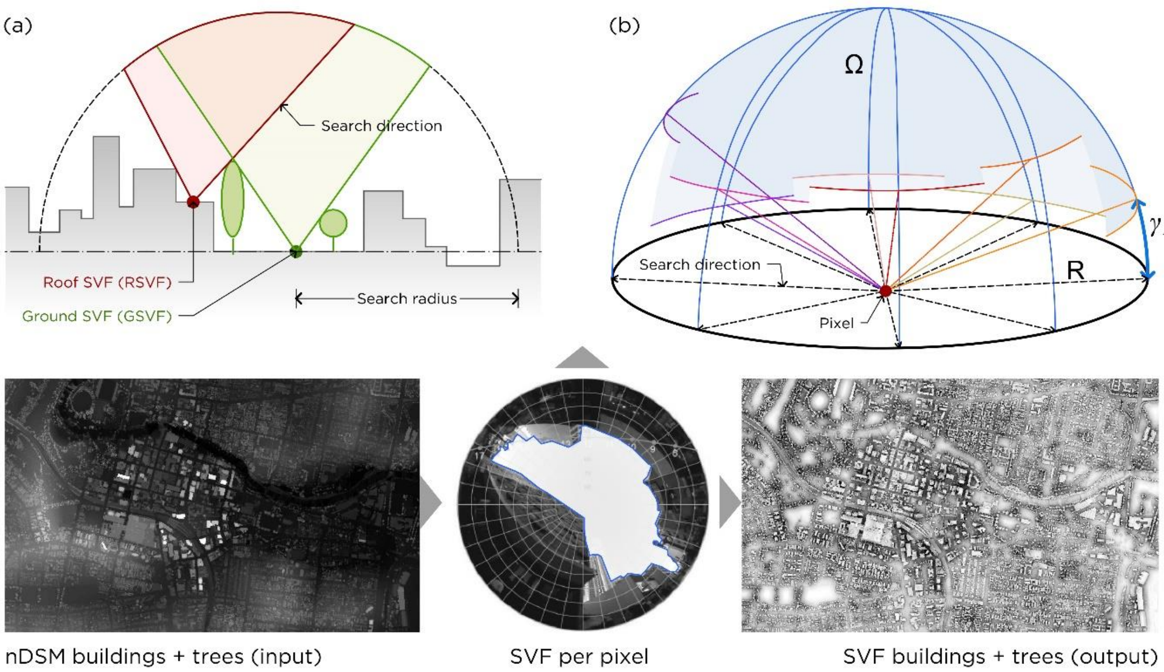

Figure 3. Estimation of GSVF and RSVF from an nDSM using RVT software: (a) value is determined as a proportion of visible sky (Ω) above certain point (pixel), and (b) the algorithm computes the horizon angle (γ) for '*n*' directions (eight in the image) in a specific search *R*.

Several empirical, analytical, and numerical methods have been developed for the estimation of SVF [75]. In this study, a digital surface model (DSM) representing ground, built and vegetation features and a digital elevation model (DEM) representing bare earth's elevations were generated from LiDAR data in CloudCompare software v2.12 [76] and subtracted from each other to produce a normalized digital surface model (nDSM) (1m resolution) representing the absolute height of buildings and trees. Continuous SVF raster images were computed in the Relief Visualization Toolbox v16.0 (RVT) software as per the method described in [77] and [78]. A raytracing radius of 50m and 32 directions were used for pixel-

[1] Values range between 0 and 1, where 1 represents an unobstructed horizon that is completely open to the sky.

based estimations as suggested by [79]. Average *GSVF* values were calculated for each spatial analytical unit by excluding buildings and top-of-the-canopy pixels, while average *RSVF* were computed by only including pixel values corresponding to roofs of buildings.

Similar studies have demonstrated that the LST profile of a given location is affected by altitude and landform, as varying intensity of solar radiation and wind channelling effects may be influenced by topographic characteristics [22, 34, 51, 80]. Accordingly, the average ground surface height (or altitude above sea level) was estimated from the LiDAR-derived DEM by computing the mean of all pixel values within each spatial analytical unit. As mentioned before, Sydney exhibits singular boundary conditions resulting from dualistic synoptic systems in which cool coastal winds play an important role [13]. To consider the potential moderating effect of sea breezes, the shortest distance (geodesic method) from the geographical centre (or centroid) of each spatial analytical unit to the nearest coastline feature was computed (from cadastral data). Only the Pacific coastline was considered in calculations and Sydney Harbour was excluded.

4.1.5 Spatial configuration of tree canopy – FRAGSTATS metrics

There are various FRAGSTATS metrics that can be employed to characterise and quantify the spatial configuration of tree canopy [26]. This study computed two normalised landscape metrics at 'class-level': (1) the 'related circumscribing circle – area weighted' (CIRCLE_AM) to measure tree patch elongation (Eq. 2), and (2) the 'normalised landscape shape index' (nLSI) to measure the aggregation or clumpiness of tree patches (Eq. 3) (Table 1). These metrics were selected based on (1) previous evaluations on most optimum combinations, (2) minimum effect from patch sizes, image resolution, grid sizes and scale, and (3) practicality and interpretability [68, 81]. Both indices were calculated for each spatial analytical unit in FRAGSTATS 4.2 software [82] using a '8-cell neighbourhood rule.

Table 1. Landscape metrics used in this study to measure the spatial pattern of trees, after [82].

Landscape metrics (Abbreviation)	Description	Equation	Eq. No.
Related circumscribing circle – area weighted (CIRCLE_AM)	Overall elongation and narrowness of a patch in relation to the whole landscape or spatial analytical unit.	$1-\left[\frac{\mathrm{a_{ij}}}{\mathrm{a_{ij}}^{s}}\right]$	(2)
Normalized Landscape Shape Index (nLSI)	Level of aggregation or clumpiness of features, hence, it can be used to distinguish between scattered and clustered trees.	$\frac{e_i-\min e_i}{\max e_i-\min e_i}$	(3)

4.2 Statistical analysis

The following sections provide the information regarding the size of the analytical units, the data integration process and the statistical and spatial modelling techniques implemented in this study.

4.2.1 *Size of spatial analytical units and data integration*

Given the pixel size of all processed data (1m) and the spatial scale of analysis (local scale), the entire landscape of the study area was divided using a regular grid of 50 x 50m cells. Each grid cell integrates all the computed variables (described in Section 3.1) and is considered as a spatial analytical unit or observation. The decision to use a 50m grid size was based on: (1) the capacity of small sampling sizes to better represent the detailed morphological and configurational characteristics of urban landscapes [11, 30, 83, 84], (2) the increasing need for fine-scale studies to better capture and analyse inter-cell spatial autocorrelation effects [8, 52], and (3) the necessity to produce a more accurate SRM and overcome the limitations of the spatial resolution from satellite imagery by using smaller sampling sizes (<120m) [14, 44, 53].

For each spatial analytical unit mean day and night LST, as response variables, were estimated using an aggregation approach [47] by averaging all pixel values within the unit extent using the zonal statistics tool in ArcGIS®. The predictor variables are the percent cover (or fraction) of surface covers, mean NDVI, GSVF, RSVF, mean altitude, distance to coast and the two landscape metrics (Figure 2). Considering the disparity between the extent and number of observations of each dataset corresponding to summer and winter (as well as day and night), the descriptive statistics for all the variables are presented in Table A1.

4.2.2 *Statistical modelling*

In this study, a number of regression models were developed to investigate the influences of various GI and urban form factors on daytime and nighttime LST in summer and winter. In order to achieve the best quality of estimations and for comparative purposes, both OLS and SRM are used. The classic OLS method was applied as it is one of the most common statistical approaches used in UHI research, with the assumption that the error terms are independent as expressed by Eq. (4):

$$y_i = \beta_0 + \beta_j x_{ij} + \varepsilon_i \qquad (4)$$

where y_i is the dependent variable (LST), β_0 is the *constant* (or intercept) of the model, β_j are the regression coefficients for *j* independent variables, x_{ij} are the independent variables and ε_i is the error term for spatial units indexed by *i*. Initially, four OLS models were developed namely, 1A – summer daytime, 2A – summer nighttime, 3A – winter daytime, and 4A winter nighttime. A *Pearson's correlation* matrix was estimated for each model to examine the magnitude, direction and significance of the linear relationships between all variables (Tables A2-A3). Guided by the results of the *Pearson's correlation*, *t-statistic* and *Variance Inflation Factor (VIF)* tests (Table A4), a new set of models (1B-4B) was developed to reduce multicollinearity between variables and to determine the best combination of variables for subsequent statistical modelling. The variance and normality of residuals (or errors) for all OLS models was assessed by the *Breusch-Pagan* [85], *Koenker-Bassett* [86], and the *Jarque-Bera* tests [87] tests..

As identified by similar studies, LST is a non-stationary geographical phenomenon that gradually varies across spatial units [88], and hence it is spatially autocorrelated [8, 14, 52, 53]. This means that the LST observed at a given location (or spatial unit) is likely to be spatially correlated with the LST observed in neighbouring cells, due to continuous surface heat exchanges and atmospheric flows [30, 44]. Since the initial OLS models tested positively for spatial autocorrelation –as determined by the *Durbin-Watson statistic* [89]– this condition was further assessed by the global autocorrelation index *Moran's I* [2] [90], and its local version known as *Local Indicators of Spatial Association* (LISA) or *Local Moran's I* [91]. SRM can account for these spatial dependences, and there are two main types, namely the Spatial Lag Model (SLM) and Spatial Error Model (SEM) [49] (Figure 4). The SLM assumes that the values of a dependent variable *y* in a specific location *i* are directly influenced by the values of *y* in neighbouring locations (*j,k*) as well as by unmeasured independent factors [92, 93]. To deal with this issue, the model incorporates a *spatially lagged term* estimated through contiguity-based spatial weights (W_{iN}) (Figure 4a) as expressed in Eq. (5):

$$y_i = x_i\beta + \rho\mathcal{W}_i y_i + \varepsilon_i \qquad (5)$$

where $\mathcal{W}_i$ is the vector (n×n) of (y_i) spatially lagged response variables, ρ is the spatial autoregressive coefficient, β are the regression coefficients of the explanatory variables, and ε_i are the independently distributed errors. In contrast, SEM models assume that spatial effects that are not fully explained by the explanatory variables are due to correlation between error terms across neighbouring locations [92, 93]. The model captures the effect of unknown predictor variables by introducing a *spatial error term* or *Lambda* (λ) which is calculated with the use of a contiguity-based spatial weights (W_{iN}) (Figure 4b) as expressed in Eq. (6):

$$y_i = x_i\beta + \lambda\mathcal{W}_i\xi_i + \varepsilon_i \qquad (6)$$

where $\mathcal{W}_i$ is the vector (n×n) of the (ξ_i) spatially lagged errors, λ is the spatial autoregressive coefficient, β are the regression coefficients of the explanatory variables, and ε_i are the independently distributed errors. A spatial weight matrix (W_{iN}) using a *first-order 'queen'* criterion of contiguity was constructed for each dataset to identify neighbouring observations with at least one point of common boundary in a regular grid (Figure 4). To compare modelling approaches and determine the appropriate model, *Lagrange Multiplier* (*LM*) statistics [94] (Table 3) were estimated as per the decision process described in [49]. The best spatial model for each dataset was chosen based on *robust LM* test results (largest *z*-

[2] Measured between -1, indicating negative spatial autocorrelation or dispersion of like-values, and +1, signalling positive spatial autocorrelation or clustering of like-values; while a value of zero signifies spatial randomness.

values) as both the *LM* test for *lag* and the LM test for error are significant (p=0.000). Revised regressions were then produced in the GeoDA v1.14 software (Anselin et al., 2006) using the SEM approach, and the maximum likelihood method.

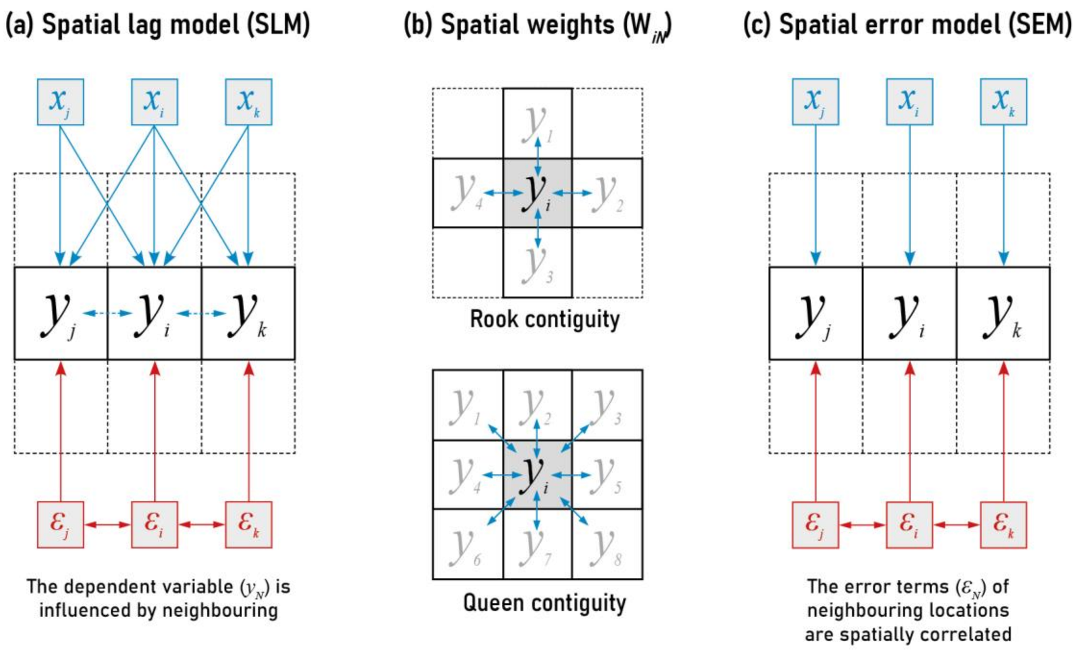

Figure 4. Differences between the spatial lag model (SLM) (a) and the Spatial Error Model (SEM) (c); and two types of contiguity-based spatial weights (b) to be estimated before choosing any of these two spatial regression models (After [93]).

5 Results

The following sections describe the results of the OLS models, the spatial autocorrelation analysis and provides a detailed comparison of the reliability and predictive performance between OLS and SRM.

5.1 Explaining the cooling effects of GI with OLS models

Initially, four OLS models (1A-4A) were produced for the prediction of daytime and nighttime LST in summer and winter in Sydney using all explanatory variables listed in Figure 2. The total number of observations used in each model corresponds to the total number of valid grid cells available for each dataset. The resulting statistics for OLS models 1A-4A are summarised in Table 2. The results indicate that the 14 explanatory variables statistically significantly predicted daytime and nighttime LSTs in summer: adj.R^2 = 0.677 (p=0.000), and adj.R^2 = 0.454 (p=0.000), as well as in winter: adj.R^2 = 0.621 (p=0.000), and adj.R^2 = 0.656 (p=0.000), respectively. Results show a weak and moderate performance for all models which is consistent with the literature.

However, initial OLS models violated several statistical assumptions suggesting stability problems that compromise their reliability and predictive power. First, the assumption of normality of residuals was violated as assessed by the *Jarque-Bera* test (p<0.001). Second, the *Durbin-Watson* statistic generated relatively low values (<1) which indicates a significant positive correlation between residuals (Table 2). Third, the results of the *Breusch-Pagan* and *Koenker-Bassett* tests show there is evidence of serious heteroscedasticity (p<0.05 for all models). Fourth, the explanatory variables are significantly correlated with each other and provide insufficient separate information as demonstrated by the very large multicollinearity condition numbers (*MCN*) (>30) (Table 2) and *VIF* (>10) and tolerance (<0.01) values (Table A4).

Pearson's correlations were performed for each model to determine which variables should be omitted to reduce multicollinearity (Tables A2-A3). Results indicate a moderate to strong correlation between *NDVI* and most surface covers as the latter were directly derived from this index. These are particularly strong in winter due to the good quality of the hyperspectral images. Considering these results and the limited contribution of *NDVI* to the explanation of thermal conditions of a cell at nighttime [64], this variable will be omitted in future. Weak to moderate negative relationships were identified between *Fr_Imp_Bld* and *Fr_Imp_Gr* and pervious covers (grasses, shrubs and trees) as the increment in the proportion of one naturally results in the decreasing of the other. Similarly, *GSVF* and *RSVF* show moderate relationships with *Fr_High_Veg* and *Fr_Imp_Bld* as both indices are directly influenced by the proportion of trees and buildings. *CIRCLE_AM* and *nLSI* are mostly uncorrelated with other predictors, yet weakly correlated with each other. *Altitude* and *D_Coast* are variables that shows no significant relationships with most variables. For each spatial unit it is assumed that all surface cover fractions sum to 100%, which means that the seven variables are perfectly collinear. Therefore, in an attempt to reduce collinearity, fraction of non-irrigated grasses (*Fr_Low_NIR*) will be omitted in subsequent regressions and becomes the reference variable.

Table 2. Summary of statistics of initial (1A-4A) and revised (1B-4B) OLS models produced for the prediction of daytime and nighttime LST in summer and winter.

Season	SUMMER				WINTER			
Time of day	Day		Night		Day		Night	
Model	1A	1B	2A	2B	3A	3B	4A	4B
Regression	Initial OLS	Revised OLS	Initial OLS	Revised OLS	Initial OLS	Revised OLS	Initial OLS	Revised OLS
N cases	23010	23010	23010	23010	24948	24948	23458	23458
R	0.823	0.821	0.674	0.644	0.788	0.788	0.810	0.806
R^2	0.678	0.675	0.454	0.415	0.621	0.621	**0.657**	**0.650**
Adj. R^2	**0.677 ***	**0.674 ***	**0.454 ***	**0.415 ***	**0.621 ***	**0.621 ***	**0.656 ***	**0.650 ***
S.E.	1.676	1.684	0.887	0.919	1.167	1.169	0.543	0.548
Log-L	**-44519.7**	**-44629.9**	**-29895.2**	**-30696.2**	**-39288.2**	**-39289.5**	**-18961.3**	**-19184.2**
AIC	**89069.4**	**89285.8**	**59820.3**	**61418.4**	**78606.5**	**78605.1**	**37952.6**	**38394.3**
SC	**89190.1**	**89390.4**	**59941.0**	**61522.9**	**78728.3**	**78710.7**	**38073.5**	**38499.1**
DW	1.01	0.992	0.852	0.790	0.799	0.800	0.901	0.891
MCN	260.26	54.9	260.26	54.9	235.62	45.7	219.32	44.1
JB	111804.8 *	114128.0 *	206986.5 *	203406.7 *	1682.2 *	1685.9 *	4314.6 *	4070.6 *
BP	26510.7 *	25140.7 *	43766.4 *	44304.3 *	2817.7 *	2713.1 *	7692.1 *	7889.3 *
KB	7272.5 *	4020.6 *	5328.5 *	5440.6 *	1792.7 *	1726.7 *	3751.8 *	3904.9 *

*S.E. = Standard error, Log-L = Log likelihood, AIC = Akaike information criterion, SC = Schwarz criterion, DW = Durbin-Watson, MCN = Multicollineatiy condition numbers, JB = Jarque-Bera, BP = Breusch-Pagan, KB = Koenker-Bassett, * p=0.000*

5.2 Revised OLS models and spatial autocorrelation analysis

Revised versions of the initial OLS models were produced using the best combination of variables guided by the results of the *MCN*, the *VIF* and *t-statistic*. A summary of statistics is presented in Table 2. There is no substantive improvement in the performance of revised models; however, multicollinearity between variables improved considerably as per lower *MCN* (<55) and *VIF* values (<7.5). Despite this, heteroscedasticity is still an issue as indicated by the large and significant values of *Breusch-Pagan* and *Koenker-Bassett* statistics (p<0.05). Non-normality of residuals is also a recurrent problem as per *Jarque-Bera* values (p<0.001). As shown by *Durbin-Watson* statistics (<1.0), there is a strong evidence of autocorrelation of residuals. These issues may be associated to: (1) the small size of grid cell (50x50m), (2) the large variation of the response variable (LST) over-small spatial units, and (3) the close proximity of spatial units which increases spatial dependencies among grid cells (particularly among residuals) [8, 14]. The latter is confirmed by the *Moran's I* and *LM* tests summarised in Table 3; which shows a statistically significant positive global spatial autocorrelation, with values >0.53 (p<0.001) and *z-values* >150 for the four revised models. This indicates a homogeneity of residuals and hence a clustering of like-values.

Table 3. Diagnostics for spatial dependence for revised OLS models (1B-4B).

Season		SUMMER		WINTER	
Time of day		Day	Night	Day	Night
Model *(response variable)*		**1B** *(DAY_T_s)*	**2B** *(NIG_T_s)*	**3B** *(DAY_T_s)*	**4B** *(NIG_T_s)*
Regression		Revised OLS	Revised OLS	Revised OLS	Revised OLS
N cases		23010	23010	24948	23458
Global Moran's I (residuals)	**MI**	**0.53**	**0.63**	**0.60**	**0.57**
	z-value	154.69	186.96	184.04	168.39
	(Sig.)	*(0.000)*	*(0.000)*	*(0.000)*	*(0.000)*
LM (lag)	z-value	8854..37	20365.53	17083.78	20905.94
	(Sig.)	*(0.000)*	*(0.000)*	*(0.000)*	*(0.000)*
Robust LM (lag)	z-value	17.0.9	12.24	1.21	323.01
	(Sig.)	*(0.000)*	*(0.0005)*	*(0.272)*	*(0.000)*
LM (error)	z-value	23855.75	34851.21	33772.85	28262.77
	(Sig.)	*(0.000)*	*(0.000)*	*(0.000)*	*(0.000)*
Robust LM (error)	z-value	15018.47	14497.91	116690.28	7679.85
	(Sig.)	*(0.000)*	*(0.000)*	*(0.000)*	*(0.000)*

Table 3 reports the statistics of the *LM* test. Both *LM-Lag* and *LM-Error* statistics are highly significant (p=0.000) for all revised OLS models. As this is commonly found in practice, *robust LM* values (p- and z-values) are considered to select the appropriate SRM [49]. Results favour SEM over SLM as the *Robust LM-Error* has a significantly higher z-value (p=0.000). *Robust LM-Error* results suggest that spatial clustering of LST is likely to be caused by geographic patterning (*i.e.* typical urban morphology) of measured explanatory variables and other unmeasured factors not in the models. Local Moran's *I* test [91] was used to identify local spatial clusters (hot- and cold-spots) of like-values that may explain the observed spatial dependence of LST. As suggested by [49], first, the typical pair of cluster and significance maps were generated using the dependent variable (LST) of each model with default permutations (*n*=9999) at a significance level (*p*=0.01) followed by a sensitivity analysis to determine the presence of spatial clusters and spatial outliers with different significance cut-off values. Second, the same LISA test was computed for residuals and results compare to those of the dependent variable. LISA values ($p<0.01$), maps and Moran scatterplots for models 1B-4B are reported in Tables A5-A8.

The high-high (HH) and low-low (LL) locations correspond to the *spatial clusters* of high and low values respectively, or areas with positive local spatial autocorrelation (clustering). On the other hand, high-low (HL) and low-high (LH) are the *spatial outliers* and represent areas with a negative local spatial autocorrelation (dispersion). A very significant positive local spatial autocorrelation of LST and residuals is identified for all models, with no significant evidence of spatial outliers in either case. As expected, the overall pattern of clusters coincides with the typical urban form of the study area, and this is likely the main cause of the spatial dependence among residuals. Accordingly, at daytime, HH clusters (hotspots) of LST typically occurred in compact, dense, and highly impervious areas, while LL clusters (cold-spots) correspond to places with large tree canopy and water surfaces. Conversely, at nighttime, hotspots comprise water bodies, compact mid- and low-rise buildings with extensive paved areas and highly forested zones; while cold-spots occur in places with extensive grasses and large low-rise buildings with light-coloured/high-albedo roofing materials. The spatial clusters from residuals occur in similar locations and follow the same pattern, however, spatial clustering of residuals is not found in areas with dense tree canopy and water surfaces.

5.3 Explaining the cooling effects of GI with the SEM model

In light of evidence of spatial autocorrelation and according to the results of *Robust LM* statistics, the SEM was chosen to predict LST using the same combination of variables selected for the revised OLS models. Four SEM models 1C-4C were produced as per Eq. (6). Results show that SEM produced higher R^2 values compared to OLS; however, this measure is not entirely appropriate as the spatial term generates a so-called *pseudo-*R^2 [49]. Instead, regression performance is assessed by *log-likelihood*, *Akaike information criterion* (*AIC*), and *Schwarz criterion* (*SC*) values. There is a considerable increase in the *log-likelihood* values and a decrease in *AIC* and *SC* estimates for all SEM models; this confirms a substantive improvement of the regressions as a result of the unmeasured variables included in the error term (λ) (Table 4). The *Likelihood Ratio* (*LR*) test enables comparison between the *null*-model (or classic regression) and the alternative SEM. The very high values and low probability ($p<0.000$) for models 1C-4C confirm the significance of the spatial autoregressive coefficient; and hence, a superior performance of SEM over OLS. This can be also corroborated by the strong and highly significant ($p<0.000$) λ coefficient for all models (>0.8). Results of *Moran's I* of residuals indicate that the introduction of the error term eliminated all spatial autocorrelation as statistics are close to zero ($p=0.001$).

Table A9 provides a comparison of regression coefficients (*β*) and significance (z- and *p*-values) for all variables included in SEM (1C-4C) versus revised OLS (1B-4B). There are slight differences in the magnitude and importance of most coefficients; however, the coefficients, and significance of *Fr_Imp_Gr*, *CIRCLE_AM, nLSI*, *GSVF*, *RSVF,* and *Altitude* have varied considerably. This illustrates the misleading effect that spatial autocorrelation has on OLS estimates and justifies the use of SRM.

Table 4. Summary of statistics of initial SEM (1C-4C), aquatic (1D-4D) and terrestrial (1E-4E) SEM models produced for the prediction of daytime and nighttime LST in summer and winter.

Season	SUMMER						WINTER					
Time of day	Day			Night			Day			Night		
Model	1C	1D	1E	2C	2D	2E	3C	3D	3E	4C	4D	4E
Regression	Initial SEM	Revised SEM	Revised SEM	Initial SEM	Revised SEM	Revised SEM	Initial SEM	Revised SEM	Revised SEM	Initial SEM	Revised SEM	Revised SEM
Context	Aquatic & Terrestrial	Aquatic	Terrestrial	Aquatic & Terrestrial	Aquatic	Terrestrial	Aquatic & Terrestrial	Aquatic	Terrestrial	Aquatic & Terrestrial	Aquatic	Terrestrial
N cases	23010	368	20331	23010	368	20331	24948	155	21020	23458	322	23458
***ρ*R²**	**0.844**	**0.867**	**0.861**	**0.799**	**0.915**	**0.802**	**0.841**	**0.640**	**0.850**	**0.870**	**0.904**	**0.883**
S.E.	1.164	0.826	0.955	0.539	0.299	0.406	0.757	0.481	0.685	0.334	0.481	0.300
Lag coef.(λ)	0.811	0.565	0.758	0.876	0.919	0.844	0.824	0.261	0.807	0.882	0.668	0.865
(Sig.)	*(0.000)*	*(0.000)*	*(0.000)*	*(0.000)*	*(0.000)*	*(0.000)*	*(0.000)*	*(0.000)*	*(0.000)*	*(0.000)*	*(0.000)*	*(0.000)*
Log-L	**-37649.2**	**-473.2**	**-29140.4**	**-20324.6**	**-168.6**	**-12166.3**	**-30166.1**	**-109.1**	**-23411.6**	**-9546.0**	**-249.5**	**-6183.8**
AIC	**75324.4**	**972.4**	**58306.9**	**40675.1**	**363.2**	**24358.5**	**60358.2**	**244.1**	**46849.2**	**19118**	**525.0**	**12393.6**
SC	**75428.9**	**1023.2**	**58409.8**	**40779.7**	**413.9**	**24461.5**	**60463.8**	**283.7**	**46952.6**	**19222.8**	**574.0**	**12496.3**
BP	20122.4	251.6	4130.2	35975.9	215.5	7910.7	5471.9	57.3	1284.0	7466.4	118.7	1004.0
(Sig.)	*(0.000)*	*(0.000)*	*(0.000)*	*(0.000)*	*(0.000)*	*(0.000)*	*(0.000)*	*(0.000)*	*(0.000)*	*(0.000)*	*(0.000)*	*(0.000)*
LR	13961.5	100.1	10335.3	20743.2	490.7	16654.5	18246.9	9.2	16029.4	19276.3	102.7	16212.5
(Sig.)	*(0.000)*	*(0.000)*	*(0.000)*	*(0.000)*	*(0.000)*	*(0.000)*	*(0.000)*	*(0.003)*	*(0.000)*	*(0.000)*	*(0.000)*	*(0.000)*
MI residuals	-0.03	-0.003	-0.06	-0.04	-0.003	-0.08	-0.06	-0.003	-0.072	-0.050	0.025	-0.070
(p-value)	*(0.001)*	*(0.18)*	*(0.001)*	*(0.001)*	*(0.001)*	*(0.001)*	*(0.001)*	*(0.46)*	*(0.001)*	*(0.001)*	*(0.259)*	*(0.001)*

ρR² = psedo-R², S.E. = Standard error, Log-L = Log likelihood, AIC = Akaike information criterion, SC = Schwarz criterion, BP = Breusch-Pagan, LR = Likelihood ratio, MI = Moran's I

Despite the favourable results from SEM, the highly significant values of *Breusch-Pagan* indicate that heteroscedasticity persists; therefore, further refinements are necessary. By taking a close look at the models' residuals, it is clear that LST from highly impervious contexts cannot be accurately predicted by the explanatory variables defined in this study, largely because the thermal condition is influenced by unobserved factors related to the morphology (*i.e.* building volume, canopy height, tree volume, etc.) and material-specific properties such as albedo, emissivity, and reflectivity. Furthermore, the distinct thermal capacity of water surfaces relative to terrestrial surfaces also partially contributed to heteroscedasticity by increasing outlying effects as suggested by similar studies [7, 52, 95]. These two conditions are captured by the spatial autocorrelation analysis described in Section 4.2 and shown in Tables A5-A8.

Since a single spatial regression equation may not be suitable for all contexts, and to minimise heteroscedasticity to the maximum extent possible, datasets were partitioned into *aquatic* observations (grid cells with *Fr_Tot_Wat* ≥ 25%), and *terrestrial* observations (grid cells with *Fr_Tot_Wat* < 25%). Since the prediction of LST in grid cells with a high proportion of impervious surfaces (*Fr_Imp_Bld* and *Fr_Imp_Gr* ≥75%) requires the introduction of material-specific predictors (i.e. albedo), these observations were also excluded from the terrestrial subset. This particular subset is subject to further investigation by including material-specific or spectral-based variables in future. SEM were recalculated to produce models 1D-4D that are applicable to aquatic locations, and models 1E-4E that are applicable to terrestrial locations using the same combination of explanatory variables defined for initial SEM models.

A statistical summary for revised SEM is presented in Table 4. Except for Model 3D, all revised SEMs exhibit a superior performance as demonstrated by the substantial improvement of *Log-Likelihood*, *AIC*, and *SC* values, as well as the reduction of standard errors (S.E.) and λ coefficients. Although heteroscedasticity is not completely eliminated, it is substantively reduced as demonstrated by the considerably smaller *Breusch-Pagan* values. Table 5 presents the regression coefficients (β_n) and significance (*z*- and *p*-values) for all explanatory variables in revised SEM models. Confidence levels have been used to determine which variables should be omitted in the final predictive equations presented in Section 5.2. As a result of data partitions, some variables became statistically insignificant for aquatic contexts. When comparing the initial SEM models and revised terrestrial models, no significant discrepancies in the magnitude and importance of most predictors, specifically the fraction of different surface covers were observed. Nonetheless, slight variations in the sign, coefficients, and significance were detected for some morphological (*GSVF*, *RSVF, Altitude, and D_Coast*) and configurational (*CIRCLE_AM, nLSI*) predictors.

5.3.1 Relative importance of explanatory variables on LST in terrestrial contexts

In terrestrial contexts, *Fr_Imp_Gr*, *Fr_Imp_Bld*, contribute the most to mean LSTs, followed by *Fr_High_Veg, Fr_Tot_Wat, and Fr_Low_IRR* across all times of the day and seasons (Table 5). In both seasons, increased *Fr_High_Veg*, *Fr_Tot_Wat*, *Fr_Low_IRR*, and *Fr_Med_Veg* (in order of importance) contribute to drops in daytime LST, while *Fr_Imp_Bld* and *Fr_Imp_Gr* significantly contribute to increases in daytime LST, and these effects are greater than the cooling capacity from GI. In contrast, nighttime LST decrease with increasing *Fr_Imp_Bld* and *Fr_Med_Veg*, while an increment in *Fr_Imp_Gr*, *Fr_High_Veg* and Fr_Tot_Wat leads to a significant increase in nighttime LST in both seasons. Whereas *Fr_Low_IRR* has a positive influence on nighttime LSTs in summer, it has a negative influence in winter. This indicates that in summer an increase in soil moisture results in a relative increment of nocturnal thermal capacity of grassed areas.

The increment in *RSVF* and *GSVF* plays a relatively important role in predicting LST in summer and winter. In both seasons, increasing *RSVF* contributes to higher LST at both times of the day, however, increasing *GSVF* has a warming effect on LST during the day while a significant cooling effect at nighttime. Furthermore, daytime and nighttime LST generally increase with increasing *Altitude,* except for summer conditions as *Altitude* shows a negative influence on nighttime LST, although this is not statistically significant (p>0.01). Distance to the coast (*D_Coast*) also has a relatively positive contribution to daytime and nighttime LST in summer, while a relatively negative contribution to daytime and nighttime LST in winter.

Table 5. Summary of regression coefficients (β) and significance (z- and p-values) for all variables included in the revised SEM applicable for aquatic (models 1D-4D) and terrestrial contexts (models 1E-4E) within the study area.

Season	SUMMER				WINTER			
Time of day	Day		Night		Day		Night	
Model	1D	1E	2D	2E	3D	3E	4D	4E
Regression	Revised SEM	Revised SEM	Revised SEM	Revised SEM	Revised SEM	Revised SEM	Revised SEM	Revised SEM
Context	Aquatic	Terrestrial	Aquatic	Terrestrial	Aquatic	Terrestrial	Aquatic	Terrestrial
$\beta_{CONSTANT}$	**37.485 *****	**29.719 *****	**18.459 *****	**20.124 *****	**6.668 *****	**10.906 *****	**4.395 *****	**3.376 *****
z-value	*20.688*	*107.925*	*20.595*	*120.821*	*5.967*	*94.946*	*4.524*	*60.718*
$\beta_{FR\_IMP\_BLD}$	**0.089 *****	**0.061 *****	**-0.017 ***	**-0.014 *****	**-0.179**	**0.034 *****	**0.090 ***	**-0.009 *****
z-value	*4.323*	*63.704*	*-2.407*	*-33.361*	*-1.371*	*50.727*	*2.377*	*-28.638*
$\beta_{FR\_IMP\_GR}$	**-0.029 ***	**0.063 *****	**0.042 *****	**0.041 *****	**-0.035**	**0.023 *****	**-0.039**	**0.018 *****
z-value	*-2.139*	*72.429*	*8.943*	*111.268*	*-1.290*	*36.091*	*-1.880*	*60.043*
$\beta_{FR\_LOW\_IRR}$	**-0.093 *****	**-0.030 *****	**0.004**	**0.002 *****	**0.023**	**-0.013 *****	**-0.016**	**-0.006 *****
z-value	*-4.612*	*-24.762*	*0.495*	*3.455*	*1.944*	*-18.250*	*-1.350*	*-17.932*
$\beta_{FR\_MED\_VEG}$	**0.011**	**-0.027 *****	**-0.002**	**-0.004 *****	**0.009**	**-0.008 *****	**0.013**	**-0.008 *****
z-value	*0.636*	*-9.768*	*-0.276*	*-3.748*	*0.865*	*-5.676*	*1.500*	*-14.094*
$\beta_{FR\_HIGH\_VEG}$	**-0.106 *****	**-0.042 *****	**0.024 *****	**0.011 *****	**0.001**	**-0.025 *****	**-0.014**	**0.012 *****
z-value	*-10.855*	*-43.354*	*7.209*	*28.256*	*0.063*	*-38.746*	*-1.549*	*42.253*
$\beta_{FR\_TOT\_WAT}$	**-0.142 *****	**-0.085 *****	**0.043 *****	**0.027 *****	**-0.021 ***	**-0.117 *****	**0.009**	**0.030 *****
z-value	-15.089	*-23.441*	*13.026*	*17.522*	*-2.306*	*-28.754*	*1.066*	*17.676*
β_{CIRCLE_AM}	**0.325**	**0.213 *****	**-0.144**	**-0.130 *****	**0.556**	**-0.223 *****	**-0.482 ****	**0.096 *****
z-value	*1.546*	*3.689*	*-1.951*	*-5.325*	*1.687*	*-5.268*	*-3.093*	*4.913*
β_{NLSI}	**0.976**	**-0.215**	**0.501**	**0.186 ****	**3.013**	**0.613 *****	**-1.238**	**-0.260 *****
z-value	*0.976*	*-1.277*	*1.528*	*2.594*	*1.467*	*4.836*	*-1.461*	*-4.687*
β_{GSVF}	**1.983 ***	**0.746 *****	**0.411**	**-0.856 *****	**1.959 *****	**2.028 *****	**1.231 ***	**-1.139 *****
z-value	*2.539*	*5.685*	*1.386*	*-15.077*	*3.657*	*25.394*	*2.398*	*-33.419*
β_{RSVF}	**-0.619**	**0.350 *****	**0.634 *****	**0.153 *****	**1.346 *****	**0.201 *****	**-0.074**	**0.056 *****
z-value	*-1.667*	*9.108*	*4.882*	*9.297*	*4.082*	*7.090*	*-0.415*	*4.351*
$\beta_{ALTITUDE}$	**-0.001**	**0.009 *****	**0.026 *****	**-0.0003**	**-0.014**	**0.005 *****	**-0.006**	**0.017 *****
z-value	*-0.121*	*8.438*	*4.078*	*-0.464*	*-1.429*	*6.613*	*-0.703*	*43.182*
β_{D_COAST}	**2.156E-005**	**0.00015 *****	**3.676E-005**	**7.819E-005 *****	**6.483E-005 ****	**-1.82E-005 *****	**-7.76E-005 *****	**-6.29E-005 *****
z-value	0.412	*15.986*	*1.168*	*12.876*	*2.753*	*-3.429*	*-5.716*	*-21.015*
β_{LAMBDA}	**0.566 *****	**0.758 *****	**0.919 *****	**0.844 *****	**0.261 *****	**0.807 *****	**0.668 *****	**0.866 *****
z-value	*13.274*	*127.782*	*84.850*	*187.976*	*3.426*	*162.548*	*17.758*	*215.132*

* $p < 0.05$, ** $p < 0.01$, *** $p < 0.001$. *Non-significant variables are greyed-out.*

It is also observed that morphology-related explanatory variables (particularly composition of surface covers) are more influential in daytime and nighttime LST than the spatial configuration of trees. Despite this, an increasing elongation of tree patches (*CIRCLE_AM*) causes a relative increment of daytime LST and a reduction of LST in summer. An inverse pattern occurs in winter, when increasing linearity of tree patches contributes to lower daytime LST and higher nighttime LST. Dispersion of tree patches (*nLSI*) is a statistically significant predictor at nighttime in summer and both day and night in winter. In summer, scattered trees can be associated with higher nighttime LST; conversely, in winter increasing dispersion of trees contributes to higher daytime LST and lower nighttime LST.

5.3.2 Relative importance of explanatory variables on LST in aquatic contexts

In aquatic contexts, *Fr_Tot_Wat* has a significantly negative effect on LST during daytime and significantly positive effects on LST during the night and became the most important predictor of LST across all times of day and seasons (Table 5). In summer, *Fr_Tot_Wat* contributes most to the reduction of daytime LST, followed by *Fr_High_Veg*, *Fr_Low_IRR and Fr_Imp_Gr*; while *Fr_Imp_Bld* and *GSVF* contribute to increase LST during the day. At nighttime, LST increases with increasing *Fr_Tot_Wat*, *Fr_Imp_Gr*, *Fr_High_Veg* as well as with increasing *RSVF* and *Altitude*, while LST decreases by increasing *Fr_Imp_Bld*. In winter, *Fr_Tot_Wat* was the only significant variable contributing to decrease daytime LST; while *RSVF, GSVF* and *D_Coast* (in order of importance) contribute to the increment of LST. During the night, LST decreases with increasing *D_Coast* and elongation of tree patches (*CIRCLE_AM*), and LST increases with increasing *Fr_Imp_Bld* and *GSVF* values.

6 Discussion

6.1 The methodological implications: the importance of selecting the appropriate statistical approach, scale and data resolution

Results in this study highlight the necessity of selecting the appropriate statistical approach to predict LST from various GI- and urban form-related factors. After several attempts to produce reliable OLS models, it was clear that there was a strong spatial autocorrelation among residuals for the initial models that was quantified by global and local Moran's *I* indices. As suggested by similar studies, our results confirm the need to incorporate the effect of spatial dependency into traditional MLR models, otherwise autocorrelation leads to model instability and misleading interpretation of estimates [30, 53]. In this regard, the use of SRM was advantageous as it increased substantially the overall goodness-of-fit of models by capturing the effect of unobserved predictors and incorporating the spatial autocorrelation as an additional explanatory variable (λ). Furthermore, as independence between observations is not required for SRM, parameter estimates are generally more reliable [30].

However, higher model performance does not necessarily imply a better understanding of the relationships between independent and dependent variables as the explanatory power of the spatial error term can be affected by a myriad of factors [30], such as the scale of observation, the size of spatial units, and the resolution of raw data, and so on. Evidence presented in this paper supports previous research which indicates that finer operational scales and analytical units contribute to an increased spatial autocorrelation as LST are more likely to be affected by adjacent locations [53]. Accordingly, higher model fitness may result from the powerful explanatory capacity of the spatial (error or lag) term. However, a past study has shown that increasing the size of grid cells may contribute to stronger relationships between spatial predictors and LST [53]. Since spatial dependency is weaker at a coarser scale, LST is less likely to be impacted by neighbouring locations [14]; therefore, OLS modelling may be more appropriate at coarser levels [52, 53]. Owing to limited data, time and resources, a multi-scale or multi-resolution evaluation on model performance was not conducted in this study, so these scale-related aspects could be incorporated into future work.

The resolution of raw imagery generally determines the size of the analytical unit. This is particularly true for satellite-based studies as the minimum analytical unit mostly coincides with the smallest resolution from image data (*i.e.* a Landsat ETM+ image of 30m produces a minimum analytical unit of 30m), so any information finer than this raw scale is missing [44]. However, this is not always the case for studies employing airborne-based imagery. This study focused on the need to implement SRM at finer scales, using VHR imagery [14]. A 50x50m grid cell was applied as analytical unit in order to capture the structure and variation of thermal conditions within a smaller spatial extent as suggested by [83]. Although this produced superior model performance –at the expense of increasing the power of the spatial error term– the results should be interpreted with caution as thermal and some physical conditions were averaged for the totality of each grid cell regardless of specific location and distribution. This applies to the estimation of *LST*, *GSVF*, *RSVF*, *Altitude* and *NDVI* as mean values result from averaging all the available pixels within each grid cell obtained from the VHR (1m) image data.

Choosing the appropriate SRM and spatial weight matrix is equally important. [30] has indicated that increasing the 'contiguity order' of the spatial weight considerably decreases the model performance. Accordingly, this research applied a *first-order queen* contiguity matrix for all models so spatial dependencies in each cell were estimated from the eight immediately adjacent neighbours. In accordance with earlier findings, the spatial association of LST at local level (LISA) induced the spatial autocorrelation among residuals in OLS models [30]. This was confirmed by the results of *robust LM* tests that showed that SEM is more suitable than SLM in dealing with such spatial dependencies. However, this may differ for other contexts (or studies) as the results of *robust LM* tests are occasionally contradictory. For instance, work similar to that presented here has preferred the use of SLM models [30] or a more general form of the spatial model (GSM) [8, 14, 44] to capture the effects of multiple autocorrelation components. These discrepancies may arise because of differences in the operational scale, the spatial resolution of imagery, the methods for retrieving LST, and the set of predictors employed.

6.2 Predicting the spatio-temporal impacts of GI and urban form on LST

This research has examined the exact contribution (or influence) of various GI- and urban form variables on daytime and nighttime LST in summer and winter. In accordance with previous studies, our results indicate that land cover composition affects LST more than spatial configuration does [14, 30, 81]. Based on the equation of SEM (Eq. 4), the relationship between daytime and nighttime LST and relevant predictors (as per Table 5) at the local scale can be explained through the following general equation (Eq. 7):

$$T_s = \beta_0 + \beta_1 Fr_{Imp_{Bld}} + \beta_2 Fr_{Imp_{Grnd}} + \beta_3 Fr_{Low_{IRR}} + \beta_3 Fr_{Med_{Veg}} + \beta_4 Fr_{High_{Veg}} + \beta_5 Fr_{Tot_{Wat}} + \beta_6 CIRCLE_{AM} + \beta_7 nLSI + \beta_8 GSVF + \beta_9 RSVF + \beta_{10} Altitude + \beta_{11} D_{Coast} + \lambda + \varepsilon_i \quad (7)$$

where T_s corresponds to the daytime and nighttime LST in a given location and season, β_0 is the model constant, β_n represents the regression coefficients of each explanatory variable, λ is the autoregressive coefficient (spatial error term), and ε_i refers to the spatially uncorrelated error term of the regression. Values in Eq. 7 can be replaced by the statistically significant regression coefficients of SEMs listed in Table 5 to derive specific equations for the prediction of LST for aquatic and terrestrial contexts across Sydney metropolitan area. The coefficient β_n of a variable *n* in the equations indicates that if the variable increases by one unit, while other variables are held constant, the predicted LST will also increase (or decrease) in β_n units. Since the fraction of non-irrigated grasses (*Fr_Low_NIR)* was excluded to avoid perfect collinearity (Section 4.1), this variable functions as reference to which other selected variables are compared. Accordingly, the increase of a surface cover fraction by a given amount will result in the decrease in *Fr_Low_NIR* by the same amount and vice versa. Taking this into consideration, Table 6 provides an estimation of the 'relative' effect that the change in each explanatory variable has on mean LST of a spatial unit in °C degrees for a specific context, time of the day and season, when all other variables are held constant.

In terrestrial locations, impervious surfaces contributed the most to increase mean daytime LST in both seasons. Accordingly, increasing by 10% the area of buildings (*Fr_Imp_Bld*) leads to mean LST increases of 0.61°C and 0.34°C in summer and winter, respectively; while an increment in impervious ground surfaces (*Fr_Imp_Gr*) by the same amount results in an increase of 0.63°C and 0.23°C in summer and winter, respectively. During the night, the same increase of *Fr_Imp_Gr* causes an increment in 0.41°C in summer and 0.18°C in winter. At night, many rooftops exhibited below average LST, resulting in a reduction of mean LST by 0.14°C in summer and 0.09°C in winter. The fact that buildings contributed to a general reduction of nighttime LST reflects the effect of material-specific properties such as emissivity, albedo, and thermal capacity/inertia as demonstrated in previous studies [96]. Indeed, this thermal variation can also be explained by the over-proportional abundance of light-coloured, high previous, or low thermal inertia roofing materials (*i.e.* corrugated metal roofs) which release heat more rapidly than typical ground-level materials (*i.e.* tiles, asphalt, bricks) that possess higher heat storage capacity and contribute to an enhanced surface warming during the night.

Furthermore, the distortion of recorded LST and significant warming conditions in certain areas may be attributed to (1) the large number of moving and stationary vehicles, –whose surfaces tend to be significantly hotter than other materials– and (2) the large proportion of asphalt and concrete, (*i.e.* highways, carparks, driveways and footpaths). This effect seems to be amplified in summer due to prevalent heatwave conditions experienced over the course of the data collection. This occurs because heatwaves exacerbate the magnitude and intensity of SUHIs by enhancing the thermal storage capacity of materials due to reduced evaporation and wind speeds [97, 98]. On the other hand, the accuracy of LST might be compromised by the application of a bulk emissivity value. In either case, the accuracy of predicted LST could be improved by identifying the individual thermal contribution of certain materials (*i.e.* bricks, metal, concrete, asphalt, etc.) and the estimation of corresponding material-specific emissivity/albedo values as implemented by [47], if such data become routinely available in future.

Table 6. Relative effect of each explanatory variable on mean daytime and nighttime LST (at local scale) in Sydney in summer and winter.

		Relative effect on mean LST in summer				Relative effect on mean LST in winter			
		Day		Night		Day		Night	
Variable	**Change**	Aquatic	Terrestrial	Aquatic	Terrestrial	Aquatic	Terrestrial	Aquatic	Terrestrial
Fr_Imp_Bld	+ 10%	+ 0.89 °C	+ 0.61 °C	– 0.17 °C	– 0.14 °C	*Insignif.*	+ 0.34 °C	+ 0.90 °C	– 0.09 °C
Fr_Imp_Gr	+ 10%	– 0.29 °C	+ 0.63 °C	+ 0.42 °C	+ 0.41 °C	*Insignif.*	+ 0.23 °C	*Insignif.*	+ 0.18 °C
Fr_Low_IRR	+ 10%	– 0.93 °C	– 0.30 °C	*Insignif.*	+ 0.02 °C	*Insignif.*	– 0.13 °C	*Insignif.*	– 0.06 °C
Fr_Med_Veg	+ 10%	*Insignif.*	– 0.27 °C	*Insignif.*	– 0.04 °C	*Insignif.*	– 0.08 °C	*Insignif.*	– 0.08 °C
Fr_High_Veg	+ 10%	– 1.06 °C	– 0.42 °C	+ 0.24 °C	+ 0.11 °C	*Insignif.*	– 0.25 °C	*Insignif.*	+ 0.12 °C
Fr_Tot_Wat	+ 10%	– 1.42 °C	– 0.85 °C	+ 0.43 °C	+ 0.27 °C	– 0.21 °C	– 1.17 °C	*Insignif.*	+ 0.30 °C
CIRCLE_AM	+ 0.1	*Insignif.*	+ 0.02 °C	*Insignif.*	– 0.01 °C	*Insignif.*	– 0.02 °C	– 0.05 °C	+ 0.01 °C
nLSI	+ 0.1	*Insignif.*	*Insignif.*	*Insignif.*	+ 0.02 °C	*Insignif.*	+ 0.06 °C	*Insignif.*	– 0.03 °C
GSVF	+ 0.1	+ 0.20 °C	+ 0.08 °C	*Insignif.*	– 0.09 °C	+ 0.20 °C	+ 0.20 °C	+ 0.12 °C	– 0.11 °C
RSVF	+ 0.1	*Insignif.*	+ 0.04 °C	+ 0.06 °C	+ 0.02 °C	+ 0.14 °C	+ 0.02 °C	*Insignif.*	+ 0.01 °C
Altitude	+ 10m	*Insignif.*	+ 0.09 °C	+ 0.26 °C	*Insignif.*	*Insignif.*	+ 0.05 °C	*Insignif.*	+ 0.17 °C
D_Coast	+ 1000m	*Insignif.*	+ 0.15 °C	*Insignif.*	+ 0.08 °C	+ 0.06 °C	– 0.02 °C	– 0.08 °C	– 0.06 °C

Insignif. = Statistically insignificant (p>0.05)

Also, in terrestrial contexts, the presence of water features (*i.e.* fountains) and tree canopy (*Fr_High_Veg*) contributed the most to reducing the mean LST during the day, where an increase of 10% in area results in a drop of 0.85°C and 0.42°C in summer, and 1.17°C and 0.25°C in winter, respectively. Surprisingly, at nighttime the magnitude of the warming effect of water and trees appears to be the same in both seasons, causing a similar increase in mean nighttime LST of 0.27-0.30°C, and 0.11-0.12°C, respectively. Given the similar nocturnal temperature moderating effect observed for water and trees, thermal differences across the study area confirm the significant role that the abundance of impervious surfaces played in defining the thermal profile of a place, particularly at night.

The cooling effect of shrubs (*Fr_Med_Veg*) on mean LST is relatively the same throughout the day in winter, with a decrease of 0.08°C per an increase of 10% in area. The cooling effects in summer, however, are more pronounced during the day (0.27°C) than during the night (0.04°C). The cooling effects of irrigated grasses (*Fr_Low_IRR*) are quite distinctive at different times of the day and seasons. In summer, a 10% increase in area results in a cooling effect of 0.30°C during the day, but a warming effect of 0.02°C at night. In contrasting, in winter an increment of the same proportion decreases daytime LST by 0.13°C and nighttime LST by 0.06°C. This behaviour is reported in the literature, so at daytime increasing surface wetness reduces LST as the evaporation of water converts sensible into latent heat, causing a cooling effect [99–101]. However, in prolonged warming conditions such as in summer (or during heatwaves), an increasing soil moisture results in an enhanced thermal capacity and higher thermal admittance, so watered surfaces may not cool as rapidly as dry plants and bare soils at night [102, 103].

As mentioned earlier, spatial predictors (*CIRCLE_AM, nLSI*) contributed the least to an explanation of the thermal condition of grid cells. This may be explained by the methodological approach implemented in this study as the LST depends on areal estimates and thermal conditions that were averaged for the totality of the spatial unit; hence, estimations are highly dependent on abundance rather than configuration [53]. This assumption, however, might be different for air temperature observations, particularly if air movement is considered. In winter, increasing tree dispersion (*nLSI*) by 0.1 units causes a slight increment in LST of 0.06°C during the day and a small decrease in LST of 0.03°C at night. In comparison, in summer no significant changes are registered during the day, with a nearly negligible warming effect at night (0.02°C). However, these findings should be interpreted with caution as TIR imagery typically represents top-of-canopy LST instead of conditions in the understory. Furthermore, it is also true that at night a compact arrangement of trees tend to trap more heat and reduce advection, which slows the liberation of the energy stored in surfaces to the open atmosphere [8]. Counter-intuitively, an increment in the elongation of tree patches (*CIRCLE_AM*) by 0.1 units provides a slight warming effect of 0.02°C during the day and an almost negligible cooling effect of 0.01°C during the night in summer. Conversely, in winter the same change results in a drop in daytime LST of 0.02°C and a rise in nighttime LST of 0.01°C. This may be attributed to the nature of the FRAGSTAT index, since *CIRCLE_AM* estimates the narrowness of a patch irrespective of its size or area, and it is not representative of the abundance of vegetation, and consequently the amount of shade provided by trees; therefore, it can hardly explain the LST of a specific area.

As suggested by [8], the effects of *GSVF* and *RSVF* on LST are analysed separately. An increment in *GSVF* by 0.1 unit causes a warming effect of 0.08°C and 0.20°C during the day, and a cooling effect of 0.09°C and 0.11°C during the night in summer and winter, respectively. Since *GSV*F represents the amount of in-canyon visible open sky at ground-level, daytime LST tend to be higher in open areas (>*GSVF*) due to increased solar exposure and limited shading from buildings and trees. Conversely, at night, LST are usually lower in open areas (>*GSVF*) due to enhanced heat dissipation through air circulation while heat entrapment is enhanced in narrow urban canyons (<GSVF) due to overriding effects [8]. On the other hand, an increment in *RSVF* by 0.1 unit results in a slight increase of daytime and nighttime LST between 0.01-0.04°C in both seasons. This can be attributed to increased solar exposure of roofed materials (irrespective of albedo or emissivity) that may cause a consistent warming effect throughout the day. Despite this, *RSVF* has shown to be less influential than *GSVF* on mean LST. This may be related to the fact that rooftops from mid- and high-rise buildings tend to be better ventilated, and rooftops from low-rise buildings may be overshadowed by surrounding trees and other buildings [23].

Increasing the average *Altitude* of a given area by 10m results in a warming effect of 0.09°C and 0.05°C during the day in summer and winter, respectively. However, at nighttime the same change in altitude causes an increment of 0.17°C in winter, while this effect is statistically insignificant in summer. Generally, higher daytime LST correspond to elevated locations due to exposure to higher solar irradiance and less overshadowing. In winter, however, lower nighttime LSTs are associated with low-lying locations (especially in hilly conditions) as solar penetration is limited during the day due to lower solar angles. As reported in similar studies, the distance to the coast (*D_Coast*) proved to play a relatively important role in defining the LST profile of a given place in Sydney [13, 22, 39, 57]. The present study found that in summer an increment of 1km from the coastline results in an increase of 0.15°C and 0.08°C in daytime and nighttime LST, respectively. Conversely, in winter, the same increment in distance to the coast causes a drop of 0.02°C and 0.06°C in daytime and nighttime LST, respectively. These results can be explained by the sustained heatwave conditions experienced during the summer data collection so westerly warm air advection from the country's interior mostly dominated over coastal breezes. Conversely, easterly cool breezes mostly dominated the period of the data collection in winter.

In aquatic locations, the contributions of predictors are different as many factors are irrelevant (statistically insignificant) for this context. In summer, a 10% increase in area of *Fr_Imp_Bld* results in an increase of 0.89°C in daytime LST, and a decrease of 0.17°C at night; while *Fr_Imp_Gr* shows an inverse effect causing a decrease of 0.29°C during the day and increment of 0.42°C at night. A similar pattern is observed for *Fr_Tot_Wat* and *Fr_High_Veg* which cause a cooling effect of 1.42°C and 1.06°C during the day, and warming effect of 0.43°C and 0.24°C at night, respectively. An increase of 10% in area of *Fr_Low_IRR* causes a considerable temperature drop of 0.93°C at daytime, while the effects are insignificant at nighttime. Furthermore, increasing *GSVF* by 0.1 unit results in an increment of 0.20°C during the day, but effects are insignificant at night. Elevating water surfaces (*Altitude*) by 10m raises mean nighttime LST by 0.26°C, although the effect of altitude is insignificant at daytime. The effect of *D_Coast* on LST is insignificant either at day or night in summer.

In winter, for a 10% increase *Fr_Tot_Wat*, there is a reduction in LST of 0.21°C during the day, surprisingly, at nighttime the effect of *Fr_Tot_Wat* is insignificant. The same increment in *Fr_Imp_Bld* contributes to an increase in nighttime LST of 0.90°C; while increased elongated tree patches (*CIRCLE_AM*) causes a temperature reduction of 0.05°C at night. An increase of *GSVF* by 0.1 units causes a warming effect of 0.20 and 0.12 at day and night, respectively. An increment of 1km in the distance from the coastline results in an increase in daytime LST of 0.06°C and a drop in nighttime LST of 0.08°C. As most aquatic locations in the winter dataset are low-lying or located at sea level, changes in elevation are not statistically significant at any time of the day.

Despite the excellent performance of SEM models for aquatic locations, the reduction in the number of predictors is accompanied by an increase in the coefficient, magnitude and significance of the spatial error term (λ), which indicates that LST are in fact better explained by unknown factors (Table 5). Moreover, relative effects and patterns estimated for aquatic contexts (Table 6) are not consistent between summer and winter. Of particular concern is the fact that nighttime LST cannot be explained by *Fr_Tot_Wat*. These issues may be attributed to: (1) the small number of observations used in *aquatic* models (155 to 368), (2) the significant thermal mixing resulting from other surfaces identified within grid cells, and (3) the small proportion of water surfaces (25-50%) available in many grid cells. Consequently, the interpretation of coefficient estimates for aquatic locations should be treated with caution. Forthcoming research should focus on developing predictive models exclusively for aquatic settings using a different set of predictors and a larger number of observations.

Interpretations of the relative thermal effects of each explanatory variable presented in Table 6 can be used to prescribe different SUHI mitigation strategies (or greening scenarios) for the reduction of average LST at local (neighbourhood) scale by modifying the proportion of surfaces and natural and man-made features. Figure 5 provides an example of the potential synergies and trade-offs between different heat mitigation strategies for a randomly selected spatial unit. This illustrates the capacity of predictive spatial modelling to test different possible climatic scenarios to inform policy and provide general directions and recommendations on the best selection, planning, design and management of suitable urban vegetation and artificial features to effectively ameliorate urban warming. Accordingly, the largest potential LST reduction at both day and night in summer are centred on replacing impervious ground and non-irrigated grasses with trees as well as greening building rooftops (scenarios 1 and 5). The provision of adequate irrigation and water features can be also beneficial during the day (scenarios 2, 3, 6 and 7), however, this may cause a relative heating effect during the night.

Measured explanatory variables			
Fr_Imp_Bld	21.98	*CIRCLE_AM*	0.726
Fr_Imp_Gr	39.45	*nLSI*	0.067
Fr_Low_NIR	27.86	*GSVF*	0.62
Fr_Low_IRR	6.05	*RSVF*	0.79
Fr_Med_Veg	4.38	*Altitude (m)*	17.33
Fr_High_Veg	1.16	*D_Coast (km)*	23.8
Fr_Tot_Wat	0.04		

SUMMER

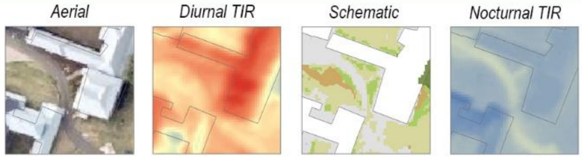

	SUHI mitigation scenarios	Effect	DAY_T_s	Effect	NIG_T_s
0	None: existing conditions	–	**40.47 °C**	–	**22.06 °C**
1	Replace all impervious ground and non-irrigated grasses with trees	↓ – 5.32 °C	35.15 °C	↓ – 0.88 °C	21.18 °C
2	Provide adequate irrigation to all current non-irrigated vegetated surfaces and bare soils	↓ – 0.84 °C	39.63 °C	↑ + 0.06 °C	22.12 °C
3	Replace all shrubs and irrigated grasses with water and provide proper irrigation to non-irrigated grasses	↓ – 1.43 °C	39.04 °C	↑ + 0.35 °C	22.41 °C
4	Replace 100% of roof area with green roofs (equivalent to well irigated grasses)	↓ – 2.00 °C	38.47 °C	↑ + 0.35 °C	22.41 °C
5	Option **1** + **4**	↓ – 7.32 °C	33.15 °C	↓ – 0.53 °C	21.53 °C
6	Option **2** + **4**	↓ – 2.84 °C	37.63 °C	↑ + 0.41 °C	22.47 °C
7	Option **3** + **4**	↓ – 3.43 °C	37.04 °C	↑ + 0.70 °C	22.76 °C

Figure 5. Example of SUHI mitigation scenarios and the potential individual and cumulative effect of various greening strategies on mean daytime and nighttime LST for a randomly selected grid in summer. Note: Colour gradation in arrows indicates the intensity of the effect.

7 Conclusions

Under a holistic approach, this paper has successfully provided novel spatially-based and multi-temporal predictive models to project the synergistic effects of GI and urban morphology characteristics on LST by accounting for spatial dependency issues at a local-scale using Sydney as case study. Results have demonstrated a superior performance of spatial regressions over traditional statistical approaches; this highlights the importance of implementing more integrated spatially-explicit approaches for the study of the impacts of greenery on the built environment.

This study has employed VHR (<2m) airborne remote sensing data to estimate LST and several spatial, morphological and functional parameters. The integration of multiple datasets represents an advance over past research as it provided a larger set of highly accurate 2D and 3D urban characteristics. Although the proposed methodology shows considerable advantages in terms of quality and accuracy of results, this study was constrained by availability, relatively high costs, and complex logistics necessary for the acquisition and processing of data. This problem is inherent to airborne remote sensing research as surveyed areas cannot always be revisited over longer periods. To tackle this issue and minimise any potential bias from confounding meteorological factors, remotely-sensed imagery was captured under the following protocols: (1) data were retrieved during the best times of the day, around noon to minimise shading effects and midnight when surfaces have lost the maximum amount of radiative energy, and for two representative seasons, summer and winter; and (2) the flight campaigns were performed under clear skies, (3) low or no wind speeds (< 2 m/s), and (4) no rainfall 72 h prior to flights. Despite these efforts, results in this study present a snapshot of specific diurnal and seasonal conditions and might not be representative for all times of the year, therefore equations should be interpreted with caution.

The interpretation of the multi-step statistical analysis and predictive modelling provided the following findings. First, the spatial association of LST at local scale (<50m) induced the spatial autocorrelation among residuals in OLS models. This confirms the need of incorporating the effect of spatial dependency into classic regression models for a reliable and accurate prediction of LST at finer scales. In this study, spatial autocorrelation analysis favoured SEM over SLM; however, this may differ for other contexts or datasets. Second, both SEM and OLS models showed significant heteroscedasticity – which is not commonly reported by other studies– that was mainly caused by: (1) the large temperature variability in areas with a very large proportion of impervious surfaces and lack of greenery –in those cases thermal conditions are influenced by unmeasured factors related to material-specific properties–, and (2) the distinct thermal behaviour of water bodies relative to terrestrial surfaces. These issues were partially solved by partitioning datasets and excluding observations corresponding to highly impervious areas (>75%). Models could be improved by incorporating albedo values of rooftop and ground-level surfaces (which is quite challenging to provide in most airborne-based studies), with particular attention to the contrasting temperatures between light-coloured and dark-coloured materials. Future research could capture the thermal variation within urban areas by segmenting datasets (or observations) into zones or classes with relatively homogenous thermal and bio-physical characteristics (to perform a comparative analysis). This can be achieved by replicating the proposed methodology using site-specific and climate-based classification schemes such as the local climate zones (LCZ) [52, 83] and its modified version the local thermal zones (LTZ) [18], the urban vegetation structure types (UVST) [104], or the green infrastructure types (GIT) [68].

Third, in terrestrial locations, imperviousness has a significant contribution in increasing mean daytime LST in both seasons. Conversely, at night, an increment of the proportion of buildings results in a reduction of mean LST, particularly in areas with mid- and high-rise buildings. This can be attributed to overshadowing from tall structures with the result that limited solar radiation penetrates the urban canyon throughout the day. The presence of water features and trees contribute the most to reduce mean LST during the day, however, the magnitude of these cooling effects does not outweigh those from impervious surfaces. At night, the increment in the proportion of water and trees causes a slight increment in mean LST in both seasons. The cooling effect of irrigated grasses is quite distinctive at different times of the day and year; for instance, in summer, increasing soil wetness resulted in an enhanced thermal capacity as watered surfaces release heat more slowly than dry plants or bare soils during the night. Thus, the effect of soil moisture deserves more attention in future models. Compared to abundance, the spatial configuration of trees has a minimal contribution to define the LST profile of a place. This may occur because the selected spatial metrics are not necessarily representative of the amount of tree cover, and hence of the amount of shade and evapotranspirative cooling.

GSVF is more influential on mean LST than *RSVF*. This may occur because thermal absorption and dissipation in rooftops is also affected by air advection at greater height or by overshadowing from taller trees and buildings. Another methodological aspect to consider is the way that *SVF* was computed. Accordingly, grid cells completely lacking roofed areas and completely covered by tree canopy were removed from *RSVF* and *GSV*F computations, respectively. In some grid cells; *null* values were assigned to both indicators (*i.e.* very dense forested areas with no buildings). Although this could have influenced regression estimates, the likelihood is a minimal impact due to the small number of cases (<1%). The effect of altitude should be interpreted in terms of topographic undulation rather than absolute elevation. Hence, higher daytime LST in summer correspond to elevated locations as there is less overshadowing, while in winter lower nighttime LST correspond to low-lying locations due to limited solar penetration. Distance to coast proved to play a relatively important role in defining the LST profile of a given place in Sydney.

Fourth, in aquatic locations, the contributions of explanatory variables are considerably different as daytime and nighttime LST mostly depend on the proportion of water, trees and unobserved factors. This is corroborated by the reduction in the number of predictors and an increase in the magnitude and significance of the spatial error term. Due to some inconsistencies in the results, it is recommended further investigations using a different set of predictors (*i.e.* material-specific properties) and larger number of aquatic observations.

This research has provided a better understanding of the effects of GI and urban form factors on LST at different times of the day and seasons. This is crucial to plan, design and implement more sustainable, liveable, and climate-adapted communities, especially in the context of climate change and global warming. With the hope of informing policy and assisting governments and practitioners, the results from spatial models can be interpreted as potential SUHI mitigation strategies at the local scale. However, this approach has limitations. For instance, the focus of this research has been on LST; however, GI as an urban living system, should be assessed holistically by considering the impacts and interactions on air temperature, thermal comfort, pollution control, and health simultaneously. Moreover, our results are not universal as estimates are based on empirical observations; therefore, future studies should consider particular climate drivers, defined by geography (*i.e.* topographic situations, latitude, hydrological conditions, and existing urban form), background climate, and regional weather. Therefore, there is no single solution that can satisfy to all possible climatic demands. Despite the attempt to consider the multi-temporal effects of GI on LST, the remote sensing methodology employed is inherently static in nature. Thus, the estimation of potential mitigation effects should consider aspects such as plant physiology, vegetation phenology, expected growing times (*i.e.* trees requiring 20-30 years to reach maturity), development of plant species resistant to higher temperatures, and future climatic conditions. Dynamic predictive approaches should be further explored (*i.e.* new advances in AI or machine learning) to deal with such level of complexities.

8 Acknowledgements

Blinded

9 References

[1] United Nations. *World Urbanization Prospects The 2011 Revision*. United Nations (UN), Population Division, Department of Economic and Social Affairs, United Nations., New York,. 2012.
[2] Santamouris, M. Regulating the damaged thermostat of the cities—Status, impacts and mitigation challenges. *Energy and Buildings*. 2015; 91:43–56.
[3] Lehmann, S. Low carbon districts. Mitigating the urban heat island with green roof infrastructure. *City, Culture and Society*. 2014; 5:1–8.
[4] Jenerette, G. D., Harlan, S. L., Buyantuev, A., Stefanov, W. L., Declet-Barreto, J., Ruddell, B. L., Myint, S. W., Kaplan, S., and Li, X. Micro-scale urban surface temperatures are related to land-cover features and residential heat related health impacts in Phoenix, AZ USA. *Landscape Ecol*. 2016.
[5] Santamouris, M. Cooling the buildings – past, present and future. *Energy and Buildings*. 2016; 128:617–38.
[6] Santamouris, M. and Osmond, P. Increasing Green Infrastructure in Cities: Impact on Ambient Temperature, Air Quality and Heat-Related Mortality and Morbidity. *Buildings*. 2020; 10,12:233.
[7] Bartesaghi-Koc, C., Osmond, P., and Peters, A. Quantifying the seasonal cooling capacity of 'green infrastructure types' (GITs). An approach to assess and mitigate surface urban heat island in Sydney, Australia. *Landscape and Urban Planning*. 2020; 203C:103893.
[8] Chun, B. and Guldmann, J.-M. Spatial statistical analysis and simulation of the urban heat island in high-density central cities. *Landscape and Urban Planning*. 2014; 125:76–88.
[9] Zhou, D., Xiao, J., Bonafoni, S., Berger, C., Deilami, K., Zhou, Y., Frolking, S., Yao, R., Qiao, Z., and Sobrino, J. Satellite Remote Sensing of Surface Urban Heat Islands: Progress, Challenges, and Perspectives. *Remote Sensing*. 2019; 11,1:48.
[10] Equere, V., Mirzaei, P. A., and Riffat, S. Definition of a new morphological parameter to improve prediction of urban heat island. *Sustainable Cities and Society*. 2020; 56:102021.
[11] Bartesaghi-Koc, C., Osmond, P., and Peters, A. Spatio-temporal patterns in green infrastructure as driver of land surface temperature variability: The case of Sydney. *International Journal of Applied Earth Observation and Geoinformation*. 2019; 83:101903.
[12] Ossola, A., Jenerette, G. D., McGrath, A., Chow, W., Hughes, L., and Leishman, M. R. Small vegetated patches greatly reduce urban surface temperature during a summer heatwave in Adelaide, Australia. *Landscape and Urban Planning*. 2021; 209:104046.
[13] Yun, G. Y., Ngarambe, J., Duhirwe, P. N., Ulpiani, G., Paolini, R., Haddad, S., Vasilakopoulou, K., and Santamouris, M. Predicting the magnitude and the characteristics of the urban heat island in coastal cities in the proximity of desert landforms. The case of Sydney. *The Science of the total environment*. 2020; 709:136068.
[14] Dai, Z., Guldmann, J.-M., and Hu, Y. Spatial regression models of park and land-use impacts on the urban heat island in central Beijing. *The Science of the total environment*. 2018; 626:1136–47.
[15] Shashua-Bar, L. and Hoffman, M. E. Vegetation as a climatic component in the design of an urban street. An empirical model for predicting the cooling effect of urban green areas with trees. *Energy and Buildings*. 2000; 31:221–35.
[16] Wang, L., Hou, H., and Weng, J. Ordinary least squares modelling of urban heat island intensity based on landscape composition and configuration: A comparative study among three megacities along the Yangtze River. *Sustainable Cities and Society*. 2020; 62:102381.
[17] Zhou, W., Qian, Y., Li, X., Li, W., and Han, L. Relationships between land cover and the surface urban heat island. Seasonal variability and effects of spatial and thematic resolution of land cover data on predicting land surface temperatures. *Landscape Ecol*. 2014; 29,1:153–67.
[18] Wang, J. and Ouyang, W. Attenuating the surface Urban Heat Island within the Local Thermal Zones through land surface modification. *Journal of environmental management*. 2017; 187:239–52.
[19] Chen, J., Zhan, W., Jin, S., Han, W., Du, P., Xia, J., Lai, J., Li, J., Liu, Z., Li, L., Huang, F., and Ding, H. Separate and combined impacts of building and tree on urban thermal environment from two- and three-dimensional perspectives. *Building and Environment*. 2021; 194:107650.
[20] Zhao, J., Zhao, X., Liang, S., Zhou, T., Du, X., Xu, P., and Wu, D. Assessing the thermal contributions of urban land cover types. *Landscape and Urban Planning*. 2020; 204:103927.

[21]Xiao, R., Weng, Q., Ouyang, Z., Li, W., Schienke, E. W., and Zhang, Z. Land Surface Temperature Variation and Major Factors in Beijing, China. *photogramm eng remote sensing*. 2008; 74,4:451–61.
[22]Irger, M. *The Effect of Urban Form on Urban Microclimate*. PhD Thesis, Faculty of Built Environment, UNSW. 2014.
[23]Morakinyo, T. E., Ouyang, W., Lau, K. K.-L., Ren, C., and Ng, E. Right tree, right place (urban canyon): Tree species selection approach for optimum urban heat mitigation - development and evaluation. *The Science of the total environment*. 2020; 719:137461.
[24]Morakinyo, T. E., Kong, L., Lau, K. K.-L., Yuan, C., and Ng, E. A study on the impact of shadow-cast and tree species on in-canyon and neighborhood's thermal comfort. *Building and Environment*. 2017; 115:1–17.
[25]Ahmadi Venhari, A., Tenpierik, M., and Taleghani, M. The role of sky view factor and urban street greenery in human thermal comfort and heat stress in a desert climate. *Journal of Arid Environments*. 2019; 166:68–76.
[26]McGarigal, K. and Marks, B. J. *FRAGSTATS. spatial pattern analysis program for quantifying landscape structure*. U.S. Department of Agriculture, Forest Service, Pacific Northwest Research Station, Portland, OR. 1995.
[27]Chen, J., Jin, S., and Du, P. Roles of horizontal and vertical tree canopy structure in mitigating daytime and nighttime urban heat island effects. *International Journal of Applied Earth Observation and Geoinformation*. 2020; 89:102060.
[28]Li, X., Li, W., Middel, A., Harlan, S. L., Brazel, A. J., and Turner, B. L. Remote sensing of the surface urban heat island and land architecture in Phoenix, Arizona: Combined effects of land composition and configuration and cadastral–demographic–economic factors. *Remote Sensing of Environment*. 2016; 174:233–43.
[29]Fan, C. and Myint, S. A comparison of spatial autocorrelation indices and landscape metrics in measuring urban landscape fragmentation. *Landscape and Urban Planning*. 2014; 121:117–28.
[30]Song, J., Du, S., Feng, X., and Guo, L. The relationships between landscape compositions and land surface temperature: Quantifying their resolution sensitivity with spatial regression models. *Landscape and Urban Planning*. 2014; 123:145–57.
[31]Cao, X., Onishi, A., Chen, J., and Imura, H. Quantifying the cool island intensity of urban parks using ASTER and IKONOS data. *Landscape and Urban Planning*. 2010; 96,4:224–31.
[32]Masoudi, M. and Tan, P. Y. Multi-year comparison of the effects of spatial pattern of urban green spaces on urban land surface temperature. *Landscape and Urban Planning*. 2019; 184:44–58.
[33]Zhou, W., Wang, J., and Cadenasso, M. L. Effects of the spatial configuration of trees on urban heat mitigation. A comparative study. *Remote Sensing of Environment*. 2017; 195:1–12.
[34]Guo, A., Yang, J., Xiao, X., Xia, J., Jin, C., and Li, X. Influences of urban spatial form on urban heat island effects at the community level in China. *Sustainable Cities and Society*. 2020; 53:101972.
[35]Bartesaghi Koc, C., Osmond, P., and Peters, A. Evaluating the cooling effects of green infrastructure: A systematic review of methods, indicators and data sources. *Solar Energy*. 2018; 166:486–508.
[36]Manesh, S. V., Tadi, M., and Zanni, F. Integrated sustainable urban design: neighbourhood design proceeded by sustainable urban morphology emergence. In *The Sustainable City VII*. WIT Transactions on Ecology and The Environment. WIT PressSouthampton, UK:631–42. 2012. DOI=10.2495/SC120532.
[37]Congedo, P. M. and Baglivo, C. Implementation hypothesis of the Apulia ITACA Protocol at district level – part I: The model. *Sustainable Cities and Society*. 2021; 70:102931.
[38]Tayyebi, A. and Jenerette, G. D. Assessing diel urban climate dynamics using a land surface temperature harmonization model. *International Journal of Remote Sensing*. 2018; 39,9:3010–28.
[39]Santamouris, M., Haddad, S., Fiorito, F., Osmond, P., Ding, L., Prasad, D., Zhai, X., and Wang, R. Urban Heat Island and Overheating Characteristics in Sydney, Australia. An Analysis of Multiyear Measurements. *Sustainability*. 2017; 9,5:712.
[40]Lee, Y. Y., Kim, J. T., and Yun, G. Y. The neural network predictive model for heat island intensity in Seoul. *Energy and Buildings*. 2016; 110:353–61.
[41]Zhou, J., Chen, Y., Wang, J., and Zhan, W. Maximum Nighttime Urban Heat Island (UHI) Intensity Simulation by Integrating Remotely Sensed Data and Meteorological Observations. *IEEE J. Sel. Top. Appl. Earth Observations Remote Sensing*. 2011; 4,1:138–46.
[42]Shandas, V., Voelkel, J., Williams, J., and Hoffman, J. Integrating Satellite and Ground Measurements for Predicting Locations of Extreme Urban Heat. *Climate*. 2019; 7,1:5.
[43]Zhang, X., Zhang, Q., Zhang, G., Nie, Z., Gui, Z., and Que, H. A Novel Hybrid Data-Driven Model for Daily Land Surface Temperature Forecasting Using Long Short-Term Memory Neural Network Based on Ensemble Empirical Mode Decomposition. *International journal of environmental research and public health*. 2018; 15,5.
[44]Wang, J., Qingming, Z., Guo, H., and Jin, Z. Characterizing the spatial dynamics of land surface temperature–impervious surface fraction relationship. *International Journal of Applied Earth Observation and Geoinformation*. 2016; 45:55–65.
[45]Declet-Barreto, J., Brazel, A. J., Martin, C. A., Chow, W. T. L., and Harlan, S. L. Creating the park cool island in an inner-city neighborhood. Heat mitigation strategy for Phoenix, AZ. *Urban Ecosyst*. 2013; 16,3:617–35.
[46]Gaitani, N., Spanou, A., Saliari, M., Synnefa, A., Vassilakopoulou, K., Papadopoulou, K., Pavlou, K., Santamouris, M., Papaioannou, M., and Lagoudaki, A. Improving the microclimate in urban areas. A case study in the centre of Athens. *Building Services Engineering Research and Technology*. 2011; 32,1:53–71.
[47]Coutts, A. M., Harris, R. J., Phan, T., Livesley, S. J., Williams, N., and Tapper, N. J. Thermal infrared remote sensing of urban heat. Hotspots, vegetation, and an assessment of techniques for use in urban planning. *Remote Sensing of Environment*. 2016; 186:637–51.

[48]Norton, B. A., Coutts, A. M., Livesley, S. J., Harris, R. J., Hunter, A. M., and Williams, N. S. Planning for cooler cities: A framework to prioritise green infrastructure to mitigate high temperatures in urban landscapes. *Landscape and Urban Planning*. 2015; 134:127–38.
[49]Anselin, L. *Exploring Spatial Data with GeoDa*. *A Workbook*. Center for Spatially Integrated Social Science, Urbana-Champaign. 2005.
[50]Chakraborti, S., Banerjee, A., Sannigrahi, S., Pramanik, S., Maiti, A., and Jha, S. Assessing the dynamic relationship among land use pattern and land surface temperature: A spatial regression approach. *Asian Geographer*. 2019; 36,2:93–116.
[51]Zhao, C., Jensen, J., Weng, Q., and Weaver, R. A Geographically Weighted Regression Analysis of the Underlying Factors Related to the Surface Urban Heat Island Phenomenon. *Remote Sensing*. 2018; 10,9:1428.
[52]Wang, Y., Zhan, Q., and Ouyang, W. How to quantify the relationship between spatial distribution of urban waterbodies and land surface temperature? *The Science of the total environment*. 2019; 671:1–9.
[53]Zhou, W., Wang, J., and Cadenasso, M. L. Effects of the spatial configuration of trees on urban heat mitigation: A comparative study. *Remote Sensing of Environment*. 2017; 195:1–12.
[54]Australian Bureau of Statistics. 2020. *Australian Statistical Geography Standard (ASGS)*. http://www.abs.gov.au/websitedbs/D3310114.nsf/home/Australian+Statistical+Geography+Standard+(ASGS). Accessed 7 March 2018.
[55]Kottek, M., Grieser, J., Beck, C., Rudolf, B., and Rubel, F. World Map of the Köppen-Geiger climate classification updated. *Meteorol. Z.* 2006; 15,3:259–63.
[56]Bureau of Meteorology. 2018. *Climate statistics for Australian locations*. http://www.bom.gov.au/climate/averages/tables/cw_066062.shtml. Accessed 22 February 2018.
[57]Bartesaghi-Koc, C., Haddad, S., Pignatta, G., Paolini, R., Prasad, D., and Santamouris, M. Can urban heat be mitigated in a single urban street? Monitoring, strategies, and performance results from a real scale redevelopment project. *Solar Energy*. 2021; 216:564–88.
[58]Bartesaghi Koc, C., Osmond, P., Peters, A., and Irger, M. A methodological framework to assess the thermal performance of green infrastructure through airborne remote sensing. *Procedia Engineering*. 2017; 180:1306–15.
[59]Santamouris, M., Ding, L., Fiorito, F., Oldfield, P., Osmond, P., Paolini, R., Prasad, D., and Synnefa, A. Passive and active cooling for the outdoor built environment – Analysis and assessment of the cooling potential of mitigation technologies using performance data from 220 large scale projects. *Solar Energy*. 2017; 154:14–33.
[60]Gillespie, A. R., Ed. *Lithologic mapping of silicate rocks using TIMS.* Jet Propulsion Laboratory Publication 86-36, Pasadena, CA. 1985.
[61]Realmuto, V. J., Ed. *Separating the effects of temperature and emissivity*. *Emissivity spectrum normalization*, Pasadena, CA: pp. 31–36. 1990.
[62]Nouri, H., Anderson, S., Beecham, S., and Bruce, D., Eds. *Estimation of Urban Evapotranspiration through Vegetation Indices Using WorldView2 Satellite Remote Sensing Images*. 2013.
[63]Nouri, H., Beecham, S., Anderson, S., and Nagler, P. High Spatial Resolution WorldView-2 Imagery for Mapping NDVI and Its Relationship to Temporal Urban Landscape Evapotranspiration Factors. *Remote Sensing*. 2014; 6,1:580–602.
[64]Weng, Q. Thermal infrared remote sensing for urban climate and environmental studies. Methods, applications, and trends. *ISPRS Journal of Photogrammetry and Remote Sensing*. 2009; 64,4:335–44.
[65]Jenks, G. F. The data model concept in statistical mapping. *International yearbook of cartography*. 1967; 7,1:186–90.
[66]Badamasi, M. M., Yelwa, S. A., AbdulRahim, M. A., and Noma, S. S. NDVI threshold classification and change detection of vegetation cover at the Falgore Game Reserve in Kano State, Nigeria. *Sokoto Journal of the Social Sciences*. 2010; 2,2:174–94.
[67]Cheng, W.-C., Chang, J.-C., Chang, C.-P., Su, Y., and Tu, T.-M. A Fixed-Threshold Approach to Generate High-Resolution Vegetation Maps for IKONOS Imagery. *Sensors*. 2008; 8,7:4308–17.
[68]Bartesaghi Koc, C., Osmond, P., and Peters, A. Mapping and classifying green infrastructure typologies for climate-related studies based on remote sensing data. *Urban Forestry & Urban Greening*. 2019; 37154-.
[69]QCoherent. *LP360. v.2012.1.22.0*. 64-Bit. 2012.
[70]Oke, T. R. Street design and urban canopy layer climate. *Energy and Buildings*. 1988; 11,1-3:103–13.
[71]Gong, F.-Y., Zeng, Z.-C., Zhang, F., Li, X., Ng, E., and Norford, L. K. Mapping sky, tree, and building view factors of street canyons in a high-density urban environment. *Building and Environment*. 2018; 134:155–67.
[72]Konarska, J., Holmer, B., Lindberg, F., and Thorsson, S. Influence of vegetation and building geometry on the spatial variations of air temperature and cooling rates in a high-latitude city. *Int. J. Climatol.* 2015:n/a-n/a.
[73]Tan, Z., Lau, K. K.-L., and Ng, E. Urban tree design approaches for mitigating daytime urban heat island effects in a high-density urban environment. *Energy and Buildings*. 2015.
[74]Unger, J. Connection between urban heat island and sky view factor approximated by a software tool on a 3D urban database. *IJEP*. 2009; 36,1/2/3:59.
[75]Chen, L., Ng, E., An, X., Ren, C., Lee, M., Wang, U., and He, Z. Sky view factor analysis of street canyons and its implications for daytime intra-urban air temperature differentials in high-rise, high-density urban areas of Hong Kong: a GIS-based simulation approach. *Int. J. Climatol.* 2012; 32,1:121–36.
[76]Girardeau-Montaut, D. *CloudCompare*. *3d Point Cloud and Mesh Processing. Open Source project*. 2021.

[77]Kokalj, Ž., Hesse, R., Cukut, J., Laharnar, B., Goldman, L., Lockett, B., Numrich, F., and Wilson, M. *Airborne laser scanning raster data visualization. A guide to good practice*. Prostor, kraj, čas / ZRC SAZU; 14. Založba ZRC, Ljubljana. 2017.
[78]Zakšek, K., Oštir, K., and Kokalj, Ž. Sky-View Factor as a Relief Visualization Technique. *Remote Sensing*. 2011; 3,12:398–415.
[79]Bartesaghi Koc, C., Osmond, P., Peters, A., and Irger, M. Mapping Local Climate Zones for urban morphology classification based on airborne remote sensing data. In *2017 Joint Urban Remote Sensing Event (JURSE)*. IEEE:1–4. 2017. DOI=10.1109/JURSE.2017.7924611.
[80]Li, S., Zhao, Z., Miaomiao, X., and Wang, Y. Investigating spatial non-stationary and scale-dependent relationships between urban surface temperature and environmental factors using geographically weighted regression. *Environmental Modelling & Software*. 2010; 25,12:1789–800.
[81]Zhou, W., Huang, G., and Cadenasso, M. L. Does spatial configuration matter? Understanding the effects of land cover pattern on land surface temperature in urban landscapes. *Landscape and Urban Planning*. 2011; 102,1:54–63.
[82]McGarigal, K., Cushman, S. A., Neel, M. C., and Ene, E. *FRAGSTATS. Spatial Pattern Analysis Program for Categorical Maps*. University of Massachusetts, Amherst (www.umass.edu/landeco/research/fragstats/fragstats.html). 2002.
[83]Stewart, I. D. and Oke, T. R. Local Climate Zones for Urban Temperature Studies. *Bull. Amer. Meteor. Soc.* 2012; 93,12:1879–900.
[84]Bechtel, B., Alexander, P., Böhner, J., Ching, J., Conrad, O., Feddema, J., Mills, G., See, L., and Stewart, I. Mapping Local Climate Zones for a Worldwide Database of the Form and Function of Cities. *IJGI*. 2015; 4,1:199–219.
[85]Breusch, T. S. and Pagan, A. R. A Simple Test for Heteroscedasticity and Random Coefficient Variation. *Econometrica*. 1979; 47,5:1287.
[86]Koenker, R. and Bassett, G. Robust Tests for Heteroscedasticity Based on Regression Quantiles. *Econometrica*. 1982; 50,1:43.
[87]Jarque, C. M. and Bera, A. K. A Test for Normality of Observations and Regression Residuals. *International Statistical Review / Revue Internationale de Statistique*. 1987; 55,2:163.
[88]Stewart, I. D. *Redefining the Urban Heat Island*. Doctor of Philosophy - PhD, University of British Columbia. 2011.
[89]Durbin, J. and Watson, G. S. *Testing for serial correlation in least squares regression. I*. Reprint series / University of Cambridge. Department of Applied Economics; no. 36. University of Cambridge, Department of Applied Economics, [Cambridge]. 1951.
[90]Moran, P. A. P. Notes on Continuous Stochastic Phenomena. *Biometrika*. 1950; 37,1/2:17.
[91]Anselin, L. Local Indicators of Spatial Association - LISA. *Geographical Analysis*. 1995; 27,2:93–115.
[92]Ward, M. and Gleditsch, K. *Spatial Regression Models*. SAGE Publications, Inc, 2455 Teller Road, Thousand Oaks California 91320 United States of America. 2008.
[93]Baller, R. D., Anselin, L., Messner, S. F., Deane, G., and Hawkins, D. F. Structural covariates of US County homicide rates. Incorporating Spatial Effects. *Criminology*. 2001; 39,3:561–88.
[94]Anselin, L. and Bera, A. K. Spatial dependence in linear regression models with an introduction to spatial econometrics. *Stat Textbooks Monogr.* 1998; 155:237–90.
[95]Zhao, C. Linking the Local Climate Zones and Land Surface Temperature to investigate the surface urban heat island, A case study of San Antonio, Texas, U.S. *ISPRS Ann. Photogramm. Remote Sens. Spatial Inf. Sci.* 2018; IV-3:277–83.
[96]Bartesaghi Koc, C., Osmond, P., Peters, A., and Irger, M. Understanding land surface temperature differences of Local Climate Zones based on airborne remote sensing data. *Journal of Selected Topics in Applied Earth Observations and Remote Sensing (JSTARS)*. 2018; 10,11.
[97]Oke, T. R., Mills, G., Christen, A., and Voogt, J. A. *Urban Climates*. Cambridge University Press. 2017.
[98]Li, D. and Bou-Zeid, E. Synergistic Interactions between Urban Heat Islands and Heat Waves: The Impact in Cities Is Larger than the Sum of Its Parts*. *J. Appl. Meteor. Climatol.* 2013; 52,9:2051–64.
[99]Erell, E., Pearlmutter, D., and Williamson, T. *Urban Microclimate. Designing the Spaces Between Buildings*. Earthscan, London, Washington, DC. 2011.
[100] Oke, T. R. *Boundary Layer Climates*. Routledge, London [England], New York. 1992.
[101] Broadbent, A. M., Coutts, A. M., Tapper, N. J., and Demuzere, M. The cooling effect of irrigation on urban microclimate during heatwave conditions. *Urban Climate*. 2018; 23:309–29.
[102] Coutts, A. M., Tapper, N. J., Beringer, J., Loughnan, M., and Demuzere, M. Watering our cities. The capacity for Water Sensitive Urban Design to support urban cooling and improve human thermal comfort in the Australian context. *Progress in Physical Geography*. 2012; 37,1:2–28.
[103] Spronken-Smith, R. A., Oke, T. R., and Lowry, W. P. Advection and the surface energy balance across an irrigated urban park. *International Journal of Climatology*. 2000; 20.
[104] Lehmann, I., Mathey, J., Rößler, S., Bräuer, A., and Goldberg, V. Urban vegetation structure types as a methodological approach for identifying ecosystem services – Application to the analysis of micro-climatic effects. *Ecological Indicators*. 2014; 42:58–72.

Appendix A. Statistical results

Table A1. Descriptive statistics for all variables estimated for each dataset in summer and winter, day and night.

Dataset	Variable*	Mean	S.D.	Minimum	Maximum	S.E.	Unit
Summer - Day & Night (*n*=23010)	*DAY_T_s*	35.8	2.95	21.2	49.4	0.20	°C
	NIG_T_s	22.6	1.20	10.5	27.7	0.01	°C
	Fr_Imp_Bld	20.0	17.66	0.0	100.0	0.12	%
	Fr_Imp_Gr	26.5	17.08	0.0	100.0	0.11	%
	Fr_Low_IRR	10.7	8.95	0.0	100.0	0.06	%
	Fr_Low_NIR	17.5	13.88	0.0	100.0	0.09	%
	Fr_Med_Veg	2.3	3.02	0.0	46.9	0.02	%
	Fr_High_Veg	22.7	19.94	0.0	100.0	0.13	%
	Fr_Tot_Wat	1.7	9.12	0.0	100.0	0.06	%
	CIRCLE_AM	0.6	0.16	0.0	1.0	0.02	N/A
	nLSI	0.1	0.06	0.0	1.0	0.00	N/A
	NDVI	-0.02	0.12	-0.7	0.6	0.00	N/A
	GSVF	0.6	0.14	0.0	0.99	0.00	N/A
	RSVF	0.6	0.31	0.0	1.0	0.00	N/A
	Altitude	34.0	27.08	0.0	131.9	0.18	m
	D_Coast	24662.9	2956.59	18952.8	31305.7	19.49	m
Winter - Day (*n*=24948)	*DAY_T_s*	12.8	1.90	6.0	21.8	0.01	°C
	Fr_Imp_Bld	22.6	18.01	0.0	100.0	0.11	%
	Fr_Imp_Gr	25.2	18.94	0.0	100.0	0.12	%
	Fr_Low_IRR	10.4	12.26	0.0	99.8	0.08	%
	Fr_Low_NIR	19.3	13.95	0.0	100.0	0.09	%
	Fr_Med_Veg	3.1	4.70	0.0	73.9	0.03	%
	Fr_High_Veg	20.3	23.27	0.0	100.0	0.15	%
	Fr_Tot_Wat	0.8	4.46	0.0	94.3	0.03	%
	CIRCLE_AM	0.6	0.19	0.0	0.9	0.00	N/A
	nLSI	0.1	0.05	0.0	1.0	0.00	N/A
	NDVI	0.4	0.20	-0.5	0.9	0.00	N/A
	GSVF	0.6	0.15	0.0	1.0	0.00	N/A
	RSVF	0.6	0.31	0.0	1.0	0.00	N/A
	Altitude	39.9	26.97	0.0	137.5	0.17	m
	D_Coast	13869.3	4644.3	4358.1	21951.5	29.4	m
Winter – Night (*n*= 23458)	*NIG_T_s*	3.2	0.93	-1.0	7.1	0.01	°C
	Fr_Imp_Bld	21.1	17.99	0.0	100.0	0.12	%
	Fr_Imp_Gr	23.2	18.97	0.0	100.0	0.12	%
	Fr_Low_IRR	10.9	12.49	0.0	100.0	0.08	%
	Fr_Low_NIR	18.6	13.88	0.0	100.0	0.09	%
	Fr_Med_Veg	3.4	5.14	0.0	74.0	0.03	%
	Fr_High_Veg	23.2	25.39	0.0	100.0	0.17	%
	Fr_Tot_Wat	1.4	9.06	0.0	100.0	0.06	%
	CIRCLE_AM	0.6	0.19	0.0	0.9	0.00	N/A
	nLSI	0.1	0.05	0.0	1.0	0.00	N/A
	NDVI	0.4	0.22	-0.7	0.9	0.00	N/A
	GSVF	0.6	0.16	0.0	1.0	0.00	N/A
	RSVF	0.6	0.32	0.0	1.0	0.00	N/A
	Altitude	51.1	39.78	0.0	193.0	0.26	m
	D_Coast	14826.5	5551.83	4018.5	28245.4	36.2	m

*See Figure 2 for explanations of abbreviations. *n* = Number of observations; *S.D.* = Standard deviation; *S.E.* = Standard error

Table A2. Pearson's correlation coefficients of variables of OLS models 1A and 2A with daytime and nighttime LST in summer as dependent variable, respectively.

SUMMER Models	T_s	Fr_Imp_Bld	Fr_Imp_Gr	Fr_Low_IRR	Fr_Low_NIR	Fr_Med_Veg	Fr_High_Veg	Fr_Tot_Wat	CIRCLE_AM	nLSI	NDVI	GSVF	RSVF	Altitude	D_Coast
1A - Daytime (*n*=23010)															
DAY_T_s	1														
Fr_Imp_Bld	.489**	1													
Fr_Imp_Gr	.480**	-.128**	1												
Fr_Low_IRR	-.107**	-.132**	-.252**	1											
Fr_Low_NIR	-.027**	-.348**	-.112**	.118**	1										
Fr_Med_Veg	-.222**	-.136**	-.204**	.042**	-.167**	1									
Fr_High_Veg	-.583**	-.385**	-.461**	-.164**	-.274**	.309**	1								
Fr_Tot_Wat	-.399**	-.156**	-.189**	-.111**	-.153**	-.010	.000	1							
CIRCLE_AM	.111**	.043**	-.009*	.009*	-.058**	.055**	.034**	-.070**	1						
nLSI	.222**	.243**	.154**	-.057**	-.071**	.029**	-.221**	-.113**	.187**	1					
NDVI	-.558**	-.444**	-.587**	.348**	-.011*	.338**	.792**	-.131**	.049**	-.250**	1				
GSVF	.212**	-.166**	.404**	.237**	.419**	-.176**	-.671**	.144**	-.120**	.071**	-.425**	1			
RSVF	.566**	.577**	.181**	.038**	-.184**	-.123**	-.428**	-.267**	.186**	.213**	-.361**	.046**	1		
Altitude	-.032**	-.021**	-.146**	.169**	-.082**	.122**	.173**	-.122**	.130**	-.030**	.222**	-.162**	.104**	1	
D_Coast	.205**	.034**	.004	.020**	.092**	.031**	-.082**	-.068**	.034**	.038**	-.043**	.031**	.067**	-.200**	1
2A - Nighttime (*n*=23010)															
NIG_T_s	1														
Fr_Imp_Bld	-.338**	1													
Fr_Imp_Gr	.431**	-.128**	1												
Fr_Low_IRR	-.168**	-.132**	-.252**	1											
Fr_Low_NIR	-.109**	-.348**	-.112**	.118**	1										
Fr_Med_Veg	-.043**	-.136**	-.204**	.042**	-.167**	1									
Fr_High_Veg	.011*	-.385**	-.461**	-.164**	-.274**	.309**	1								
Fr_Tot_Wat	.166**	-.156**	-.189**	-.111**	-.153**	-.010	.000	1							
CIRCLE_AM	.120**	.043**	-.009*	.009*	-.058**	.055**	.034**	-.070**	1						
nLSI	-.007	.243**	.154**	-.057**	-.071**	.029**	-.221**	-.113**	.187**	1					
NDVI	-.062**	-.444**	-.587**	.348**	-.011*	.338**	.792**	-.131**	.049**	-.250**	1				
GSVF	.096**	-.166**	.404**	.237**	.419**	-.176**	-.671**	.144**	-.120**	.071**	-.425**	1			
RSVF	-.026**	.577**	.181**	.038**	-.184**	-.123**	-.428**	-.267**	.186**	.213**	-.361**	.046**	1		
Altitude	-.078**	-.021**	-.146**	.169**	-.082**	.122**	.173**	-.122**	.130**	-.030**	.222**	-.162**	.104**	1	
D_Coast	.174**	.034**	.004	.020**	.092**	.031**	-.082**	-.068**	.034**	.038**	-.043**	.031**	.067**	-.200**	1

* $p < 0.05$ level (1-tailed), ** $p < 0.01$ level (1-tailed), Darker cells indicate a stronger correlation between variables.

Table A3. Pearson's correlation coefficients of variables of OLS models 3A and 4A with daytime and nighttime LST in winter as dependent variable, respectively.

WINTER Models	***T*s**	***Fr_Imp_Bld***	***Fr_Imp_Gr***	***Fr_Low_IRR***	***Fr_Low_NIR***	***Fr_Med_Veg***	***Fr_High_Veg***	***Fr_Tot_Wat***	***CIRCLE_AM***	***nLSI***	***NDVI***	***GSVF***	***RSVF***	***Altitude***	***D_Coast***
1A - Daytime (*n*=23010)															
***DAY_T*s**	1														
Fr_Imp_Bld	.531**	1													
Fr_Imp_Gr	.467**	.030**	1												
Fr_Low_IRR	-.240**	-.333**	-.372**	1											
Fr_Low_NIR	.088**	-.291**	-.104**	.107**	1										
Fr_Med_Veg	-.372**	-.233**	-.316**	-.072**	-.200**	1									
Fr_High_Veg	-.678**	-.428**	-.563**	-.027**	-.325**	.546**	1								
Fr_Tot_Wat	-.197**	-.074**	-.046**	-.040**	-.120**	-.004	.000	1							
CIRCLE_AM	-.030**	.081**	-.151**	.109**	-.110**	.036**	.052**	.002	1						
nLSI	.164**	.180**	.085**	-.076**	-.050**	.092**	-.140**	-.065**	.347**	1					
NDVI	-.676**	-.609**	-.726**	.466**	.058**	.443**	.800**	-.138**	.116**	-.138**	1				
GSVF	.382**	-.130**	.399**	.187**	.527**	-.314**	-.643**	.000	-.252**	.014*	-.344**	1			
RSVF	.503**	.633**	.222**	-.215**	-.116**	-.254**	-.468**	-.136**	.282**	.265**	-.511**	-.015**	1		
Altitude	-.078**	-.036**	-.191**	.063**	-.069**	.082**	.209**	-.125**	.231**	-.019**	.243**	-.250**	.051**	1	
D_Coast	-.071**	-.214**	-.050**	.165**	.242**	.030**	-.029**	-.035**	-.105**	.000	.134**	.234**	-.105**	.038**	1
2A - Nighttime (*n*=23010)															
***NIG_T*s**	1														
Fr_Imp_Bld	-.096**	1													
Fr_Imp_Gr	.068**	.089**	1												
Fr_Low_IRR	-.199**	-.310**	-.345**	1											
Fr_Low_NIR	-.293**	-.226**	-.030**	.110**	1										
Fr_Med_Veg	-.053**	-.248**	-.324**	-.077**	-.222**	1									
Fr_High_Veg	.199**	-.448**	-.577**	-.052**	-.368**	.541**	1								
Fr_Tot_Wat	.237**	-.122**	-.112**	-.083**	-.151**	-.036**	-.060**	1							
CIRCLE_AM	.139**	.091**	-.104**	.140**	-.063**	.023**	.013*	-.143**	1						
nLSI	-.098**	.175**	.101**	-.084**	-.038**	.102**	-.110**	-.110**	.321**	1					
NDVI	.007	-.579**	-.690**	.426**	.000	.448**	.807**	-.278**	.122**	-.106**	1				
GSVF	-.340**	-.078**	.407**	.174**	.509**	-.324**	-.674**	.158**	-.212**	.014**	-.432*	1			
RSVF	.011**	.646**	.279**	-.188**	-.037**	-.270**	-.491**	-.192**	.310**	.248**	-.483**	.040**	1		
Altitude	.506**	-.071**	-.230**	.118**	-.072**	.092**	.248**	-.151**	.230**	-.039**	.321**	-.299**	.012*	1	
D_Coast	-.107**	-.205**	-.126**	.153**	.154**	.064**	.110**	-.112**	-.015**	-.027**	.239**	.009	-.116**	.411**	1

* *p* < 0.05 level (1-tailed), ** *p*< 0.01 level (1-tailed), Darker cells indicate a stronger correlation between variables.

Table A4. Summary of *t*- and *collinearity* statistics generated for the initial (1A-4A) and revised (1B-4B) OLS models for the prediction of daytime and nighttime LST in summer and winter using all explanatory variables.

Season	Model (time of day)	Collinearity t-Statistics	*Fr_Imp_Bld*	*Fr_Imp_Gr*	*Fr_Low_IRR*	*Fr_Low_NIR*	*Fr_Med_Veg*	*Fr_High_Veg*	*Fr_Tot_Wat*	*CIRCLE_AM*	*nLSI*	*NDVI*	*GSVF*	*RSVF*	*Altitude*	*D_Coast*
Summer	**1A (Day)**	**VIF** *(Tolerance)*	163.4 *(.006)*	158.5 *(.006)*	45.9 *(.022)*	104.4 *(.010)*	3.2 *(.316)*	202.5 *(.005)*	46.1 *(.022)*	1.1 *(.889)*	1.2 *(.844)*	10.6 *(.094)*	3.2 *(.317)*	1.9 *(.508)*	1.2 *(.831)*	1.1 *(.928)*
		t *(Sig.)*	18.0 *(.000)*	18.4 *(.000)*	6.1 *(.000)*	11.7 *(.000)*	3.9 *(.000)*	4.6 *(.000)*	2.2 *(.029)*	15.8 *(.000)*	-8.7 *(.000)*	9.4 *(.000)*	-0.3 *(.799)*	25.2 *(.000)*	16.3 *(.000)*	41.0 *(.000)*
	1B (Night)	**VIF** *(Tolerance)*	3.4 *(.292)*	2.6 *(.382)*	1.8 *(.569)*		1.2 *(.872)*	5.2 *(.191)*	1.4 *(.733)*	1.1 *(.893)*	1.2 *(.856)*		3.1 *(.325)*	2.0 *(.514)*	1.2 *(.835)*	1.1 *(.929)*
		t *(Sig.)*	40.8 *(.000)*	47.7 *(.000)*	-19.2 *(.000)*		-7.6 *(.000)*	-33.3 *(.000)*	-58.5 *(.000)*	16.3 *(.000)*	-8.5 *(.000)*		1.9 *(.049)*	25.8 *(.000)*	15.6 *(.000)*	40.6 *(.000)*
	2A (Day)	**VIF** *(Tolerance)*	162.4 *(.006)*	158.5 *(.006)*	45.9 *(.022)*	104.4 *(.010)*	3.2 *(.316)*	202.5 *(.005)*	46.1 *(.022)*	1.1 *(.889)*	1.2 *(.844)*	10.6 *(.094)*	3.2 *(.317)*	1.9 *(.508)*	1.2 *(.831)*	1.1 *(.928)*
		t *(Sig.)*	9.9 *(.000)*	23.9 *(.000)*	6.3 *(.000)*	12.5 *(.000)*	2.8 *(.005)*	8.7 *(.029)*	24.9 *(.000)*	17.8 *(.000)*	1.9 *(.063)*	39.1 *(.000)*	-17.9 *(.000)*	19.7 *(.000)*	2.2 *(.031)*	41.6 *(.000)*
	2B (Night)	**VIF** *(Tolerance)*	3.4 *(.292)*	2.6 *(.382)*	1.8 *(.569)*		1.2 *(.872)*	5.2 *(.191)*	1.4 *(.733)*	1.1 *(.893)*	1.2 *(.856)*		3.1 *(.325)*	2.0 *(.514)*	1.2 *(.835)*	1.1 *(.929)*
		t *(Sig.)*	-29.3 *(.000)*	66.9 *(.000)*	1.8 *(.063)*		-6.1 *(.000)*	15.9 *(.000)*	52.0 *(.000)*	19.8 *(.000)*	-0.5 *(.615)*		-11.5 *(.000)*	22.8 *(.000)*	-0.5 *(.643)*	39.3 *(.000)*
Winter	**3A (Night)**	**VIF** *(Tolerance)*	132.6 *(.008)*	149.1 *(.007)*	61.9 *(.016)*	77.9 *(.013)*	2.7 *(.369)*	203.3 *(.005)*	10.1 *(.099)*	1.6 *(.636)*	1.3 *(.776)*	41.4 *(.024)*	3.2 *(.316)*	2.3 *(.435)*	1.2 *(.838)*	1.2 *(.866)*
		t *(Sig.)*	7.9 *(.000)*	3.6 *(.000)*	-3.9 *(.000)*	0.2 *(.873)*	-3.5 *(.001)*	-5.1 *(.000)*	-11.7 *(.000)*	1.5 *(.128)*	2.9 *(.004)*	1.6 *(.107)*	33.1 *(.000)*	11.8 *(.000)*	14.7 *(.000)*	-8.4 *(.000)*
	3B (Day)	**VIF** *(Tolerance)*	3.7 *(.273)*	3.1 *(.326)*	2.2 *(.458)*		1.5 *(.658)*	6.7 *(.149)*	1.1 *(.907)*	1.5 *(.672)*	1.3 *(.780)*		3.1 *(.323)*	2.2 *(.449)*	1.2 *(.858)*	1.2 *(.869)*
		t *(Sig.)*	44.3 *(.000)*	21.5 *(.000)*	-20.2 *(.000)*		-4.6 *(.001)*	-27.3 *(.000)*	-37.6 *(.000)*	1.8 *(.069)*	3.0 *(.003)*		33.7 *(.000)*	12.2 *(.000)*	15.1 *(.000)*	-8.3 *(.000)*
	4A (Night)	**VIF** *(Tolerance)*	115.1 *(.009)*	130.5 *(.008)*	56.1 *(.018)*	67.2 *(.015)*	2.7 *(.375)*	209.7 *(.005)*	33.9 *(.029)*	1.5 *(.651)*	1.3 *(.803)*	41.0 *(.024)*	3.3 *(.307)*	2.4 *(.416)*	1.5 *(.663)*	1.3 *(.753)*
		t *(Sig.)*	-3.5 *(.000)*	8.7 *(.000)*	-9.6 *(.000)*	-3.4 *(.001)*	-29.1 *(.000)*	-5.6 *(.000)*	20.6 *(.000)*	2.9 *(.004)*	-10.7 *(.000)*	20.8 *(.000)*	-48.2 *(.000)*	8.8 *(.000)*	133.5 *(.000)*	-68.9 *(.000)*
	4B (Night)	**VIF** *(Tolerance)*	3.7 *(.267)*	3.3 *(.307)*	2.3 *(.438)*		1.5 *(.668)*	7.5 *(.134)*	1.4 *(.731)*	1.5 *(.679)*	1.2 *(.806)*		3.2 *(.313)*	2.4 *(.426)*	1.5 *(.690)*	1.3 *(.756)*
		t *(Sig.)*	-24.6 *(.000)*	46.9 *(.000)*	-15.3 *(.000)*		-33.8 *(.000)*	-9.4 *(.000)*	81.9 *(.000)*	6.4 *(.004)*	-10.2 *(.000)*		-45.5 *(.000)*	11.7 *(.000)*	139.0 *(.000)*	-68.6 *(.000)*

Table A5. LISA results for the dependent variable (LST) of revised OLS models 1B and 2B showing the presence of spatial clusters (hot-/cold-spots) in summer.

	Season	**SUMMER**	
	Time of day	**Day**	**Night**
	Model	**1B**	**2B**
	Regression	Revised OLS	Revised OLS
	N cases	23010	23010
LISA - LST	**Local Moran's I** z-value *(pseudo p-value)*	**0.61** 179.80 *(0.000)*	**0.53** 158.83 *(0.000)*
	Moran Scatterplot	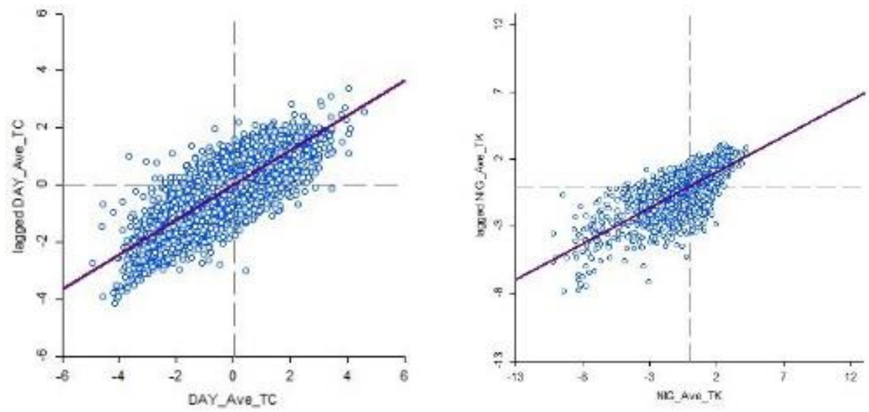	
	Cluster Map *HH in red* *LL in blue*	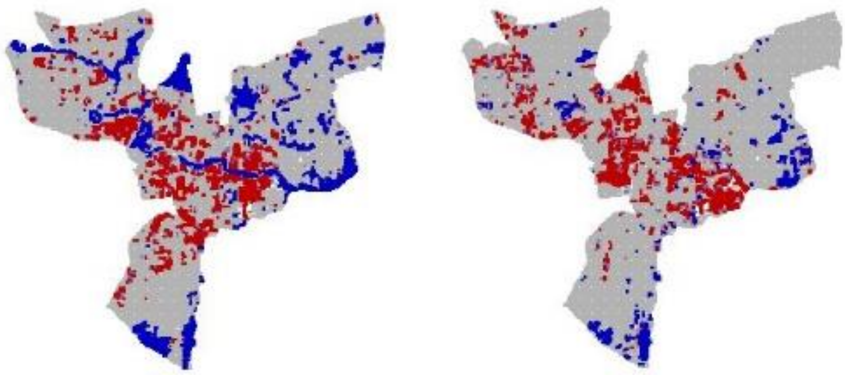	
	Significance Map (*p*<0.01)	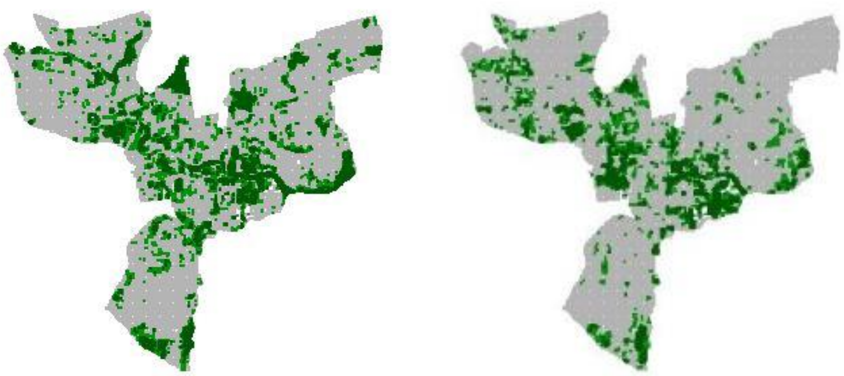	

Table A6. LISA results for the residuals of revised OLS models 1B and 2B showing the presence of spatial clusters (hot-/cold-spots) in summer.

	Season	**SUMMER**	
	Time of day	**Day**	**Night**
	Model	**1B**	**2B**
	Regression	Revised OLS	Revised OLS
	N cases	23010	23010
	Local Moran's I z-value *(pseudo p-value)*	**0.53** 153.69 *(0.000)*	**0.63** 187.60 *(0.000)*
LISA - RESIDUALS	Moran Scatterplot	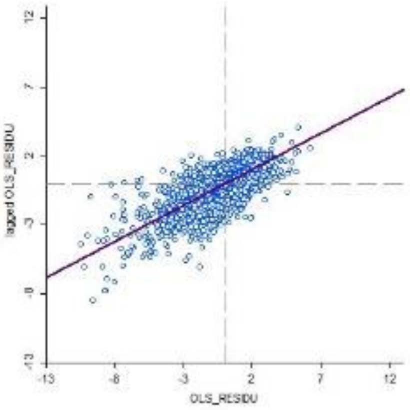	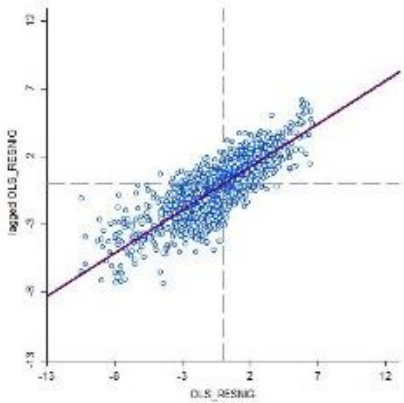
	Cluster Map *HH in red* *LL in blue*	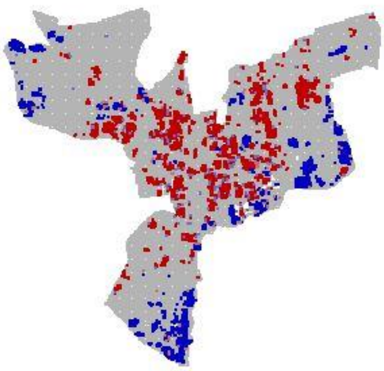	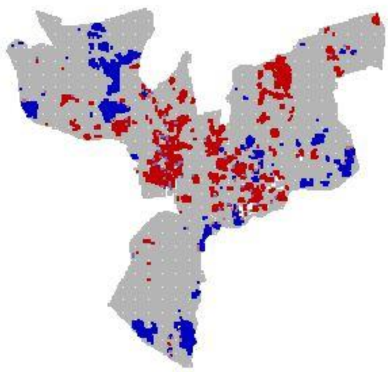
	Significance Map (*p*<0.01)	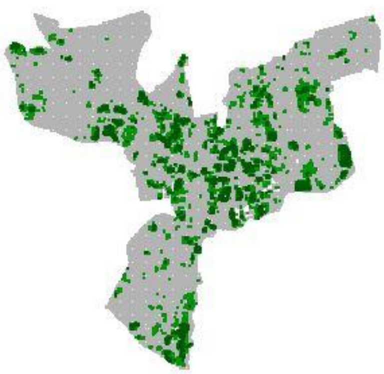	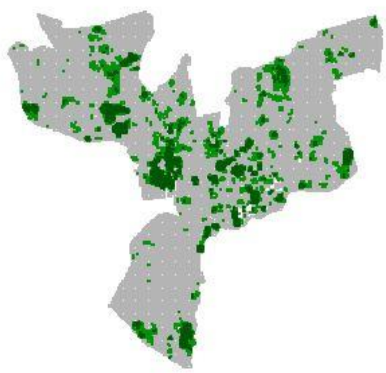

Table A7. LISA results for the dependent variable (LST) of revised OLS models 3B and 4B showing the presence of spatial clusters (hot-/cold-spots) in winter.

	Season	WINTER	
	Time of day	Day	Night
	Model	**3B**	**4B**
	Regression	Revised OLS	Revised OLS
	N cases	24948	23458
	Local Moran's I z-value *(pseudo p-value)*	**0.68** 210.67 *(0.000)*	**0.74** 222.86 *(0.000)*
LISA - LST	Moran Scatterplot	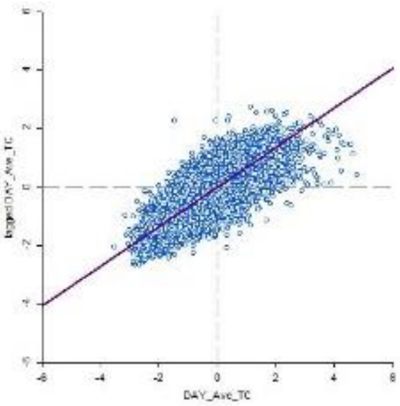	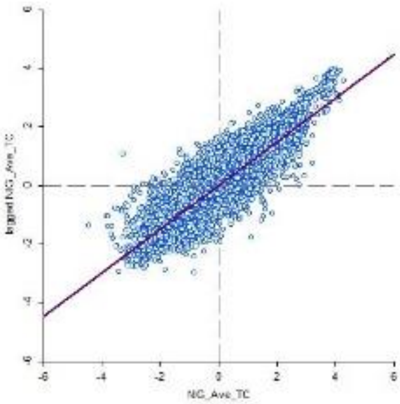
	Cluster Map *HH in red* *LL in blue*	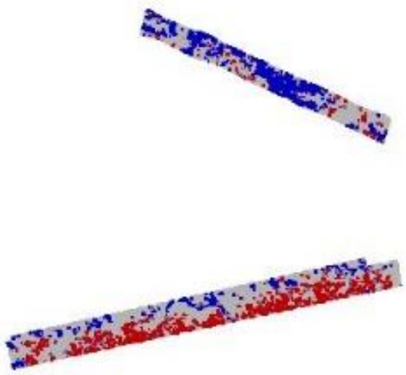	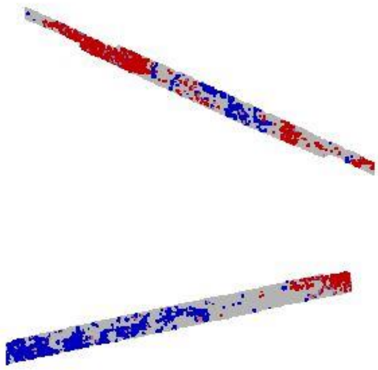
	Significance Map (*p*<0.01)		

Table A8. LISA results for the residuals of revised OLS models 3B and 4B showing the presence of spatial clusters (hot-/cold-spots) in winter.

	Season	WINTER	
	Time of day	**Day**	**Night**
	Model	**3B**	**4B**
	Regression	Revised OLS	Revised OLS
	N cases	24948	23458
	Local Moran's I z-value *(pseudo p-value)*	**0.59** 185.32 *(0.000)*	**0.57** 169.44 *(0.000)*
LISA - LST	Moran Scatterplot	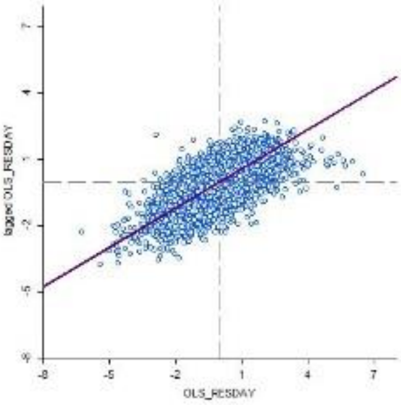	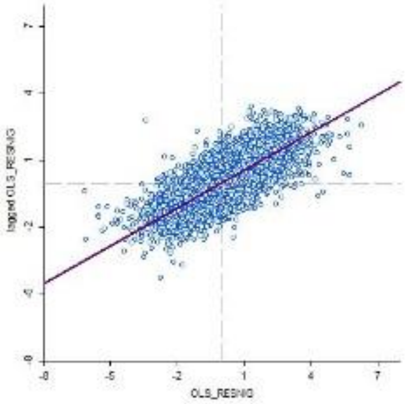
	Cluster Map *HH in red* *LL in blue*	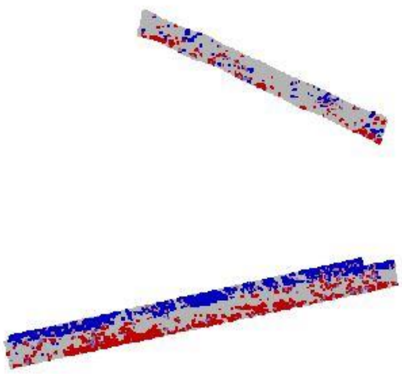	
	Significance Map (*p*<0.01)		

Table A9. Comparison of regression coefficients (β) and significance (*z*- and *p*-values) for all variables included in the revised OLS models (1B-4B) and initial SEM models (1C-4C) applicable to the entire study area.

Season	SUMMER				WINTER			
Time of day	Day		Night		Day		Night	
Model	1B	1C	2B	2C	3B	3C	4B	4C
Regression	Revised OLS	Initial SEM	Revised OLS	Initial SEM	Revised OLS	Initial SEM	Revised OLS	Initial SEM
β_{CONSTANT}	**29.291 *****	**29.559 *****	**19.311*****	**19.565 *****	**10.171 *****	**10.835 *****	**3.957 *****	**3.373 *****
z-value	*161.331*	*77.282*	*194.882*	*75.732*	*99.812*	*90.151*	*82.442*	*53.396*
$\beta_{\text{FR\_IMP\_BLD}}$	**0.048 *****	**0.052 *****	**-0.019 *****	**-0.019 *****	**0.035 *****	**0.037 *****	**-0.009 *****	**-0.010 *****
z-value	*40.818*	*53.231*	*-29.268*	*-41.732*	*44.304*	*60.751*	*-24.589*	*-37.147*
$\beta_{\text{FR\_IMP\_GR}}$	**0.050 *****	**0.056 *****	**0.038 *****	**0.039 *****	**0.015 *****	**0.022 *****	**0.016 *****	**0.016 *****
z-value	*47.672*	*56.751*	*66.949*	*85.603*	*21.511*	*36.649*	*46.871*	*56.345*
$\beta_{\text{FR\_LOW\_IRR}}$	**-0.032 *****	**-0.032 *****	**0.002**	**0.002 ****	**-0.018 *****	**-0.013 *****	**-0.007 *****	**-0.006 *****
z-value	*-19.164*	*-22.188*	*1.862*	*2.951*	*-20.165*	*-17.470*	*-15.250*	*-17.796*
$\beta_{\text{FR\_MED\_VEG}}$	**-0.030 *****	**-0.022 *****	**-0.013 *****	**-0.002 *****	**-0.009 *****	**-0.008 *****	**-0.029 *****	**-0.008 *****
z-value	*-7.596*	*-6.714*	*-6.091*	*-1.477*	*-4.636*	*-5.359*	*-33.751*	*-12.028*
$\beta_{\text{FR\_HIGH\_VEG}}$	**-0.042 *****	**-0.046 *****	**0.011 *****	**0.013 *****	**-0.023 *****	**-0.025 *****	**0.004 *****	**0.011 *****
z-value	*-33.338*	*-43.354*	*15.891*	*26.861*	*-27.266*	*-37.506*	*9.382*	*39.863*
$\beta_{\text{FR\_TOT\_WAT}}$	**-0.083 *****	**-0.086 *****	**0.040 *****	**0.034 *****	**-0.065 *****	**-0.061 *****	**0.038 *****	**0.029 *****
z-value	*-58.479*	*-56.156*	*52.031*	*47.240*	*-37.548*	*-43.517*	*81.874*	*53.842*
$\beta_{\text{CIRCLE\_AM}}$	**1.217 *****	**0.323 *****	**0.804 *****	**0.125 *****	**0.087**	**-0.271 *****	**0.146 *****	**0.119 *****
z-value	*16.318*	*5.754*	*19.751*	*4.832*	*1.821*	*-7.508*	*6.394*	*7.164*
β_{NLSI}	**-1.641 *****	**-0.672 *****	**-0.052**	**0.079**	**0.505 ****	**0.370 ****	**-0.828 *****	**-0.219 *****
z-value	*-8.537*	*-4.606*	*-0.503*	*1.173*	*2.966*	*3.094*	*-10.233*	*-4.075*
β_{GSVF}	**0.282 ***	**0.607 *****	**-0.896 *****	**-0.419 *****	**3.020 *****	**2.009 *****	**-1.874 *****	**-0.998 *****
z-value	*1.973*	*4.757*	*-11.469*	*-7.027*	*33.657*	*25.720*	*-45.496*	*-29.505*
β_{RSVF}	**1.280 *****	**0.439 *****	**0.617 *****	**0.233 *****	**0.430 *****	**0.155 *****	**0.200 *****	**0.063 *****
z-value	*25.822*	*10.045*	*22.797*	*11.426*	*12.151*	*5.284*	*11.725*	*4.700*
β_{ALTITUDE}	**0.007 *****	**0.011 *****	**-0.00011**	**0.0006**	**0.005 *****	**0.005 *****	**0.015 *****	**0.017 *****
z-value	15.640	*7.612*	*-0.464*	*0.618*	*15.111*	*5.456*	*138.998*	*36.634*
$\beta_{\text{D\_COAST}}$	**0.00015 *****	**0.00017 *****	**8.361E-005 *****	**8.360E-005 *****	**-1.42E-005 *****	**1.006E-005**	**-5.086E-005 *****	**-6.55E-005 *****
z-value	*40.657*	*12.010*	*39.324*	*8.530*	*-8.304*	*-1.702*	*-68.564*	*-18.153*
β_{LAMBDA}	N/A	**0.811 *****	N/A	**0.876 *****	N/A	**0.824**	N/A	**0.882 *****
z-value		*157.566*		*218.611*		*173.38*		*231.998*

* $p < 0.05$, ** $p < 0.01$, *** $p < 0.001$. *Non-significant variables are greyed-out.*